LA-9436-MS

UC-79p
Issued: August 1982

LA--9436-MS

DE82 021255

Intersubassembly Fuel Penetration into a Failed Blanket Subassembly

G. P. DeVault
C. R. Bell

Los Alamos National Laboratory
Los Alamos, New Mexico 87545

CONTENTS

LIST OF FIGURES

LIST OF TABLES

INTERSUBASSEMBLY FUEL PENETRATION INTO A FAILED BLANKET SUBASSEMBLY

by

G. P. DeVault and C. R. Bell

ABSTRACT

This work provides additional understanding of hypothetical core-disruptive accident issues involving LMFBRs. Intersubassembly molten fuel and steel penetration into a failed blanket subassembly was analyzed with the two-dimensional SIMMER-II code. Interaction of the fuel and steel with the blanket coolant was included in the investigation. The molten core material was injected through a prescribed opening in the blanket subassembly wall. Eighteen cases involving variations of parameters of importance to the subsequent flow were calculated. In general the resulting pressurization was a good figure of merit for rating the severity of the events. In turn, the pressurization depended on the wall opening size, the initial pool pressure, and the heat-transfer rates. However, only when the wall failure rate was large relative to the sodium expulsion rate, was sufficient pressure generated that could affect the reactor vessel containment.

I. INTRODUCTION

This report is one of a series designed to provide additional understanding of generic hypothetical core-disruptive accident (HCDA) issues that would be of benefit to Clinch River Breeder Reactor (CRBR) safety assessment as well as for assessment of other reactors.[1] This work examined the possible effects of penetration from a molten fuel pool into an intact, sodium-filled blanket subassembly on the postdisassembly expansion work potential of the molten pool. Several effects were possible. Any sodium vapor introduced into the pool by the interaction would behave like a noncondensable gas, adding its own work potential to that of the pool materials. As a mitigating effect, the expulsion of sodium from the subassembly would result in some removal of quenched molten materials that would reduce the work potential of the pool.

For this work a single intact radial blanket subassembly that had survived the initiating phase and early transition phase of an HCDA was considered. This subassembly had as its external environment a stationary pool of molten fuel, molten steel, and sodium vapor representing six adjacent, disrupted driver subassemblies. Subsequent heating of the blanket subassembly wall caused it to fail, allowing pool material to be injected through the opening and to interact with sodium within the pin bundle geometry. The subsequent blanket sodium expulsion axially and through the opening was investigated through general parametric studies performed with SIMMER-II to explore general trends and first-order sensitivities. SIMMER-II[2] is a two-dimensional coupled neutronics fluid-dynamics code intended for transition phase, core disassembly, and extended fuel motion analysis related to postulated liquid-metal-cooled-fast-breeder-reactor (LMFBR) HCDAs.

This work was exploratory only and recommendations have been made for future analyses.

II. GEOMETRY AND INITIALIZATION

For these studies a typical internal blanket subassembly from the CRBR heterogeneous core was chosen (see Fig. 1). This blanket subassembly was assumed to be surrounded by driver subassemblies that had become severely disrupted during a postulated HCDA.

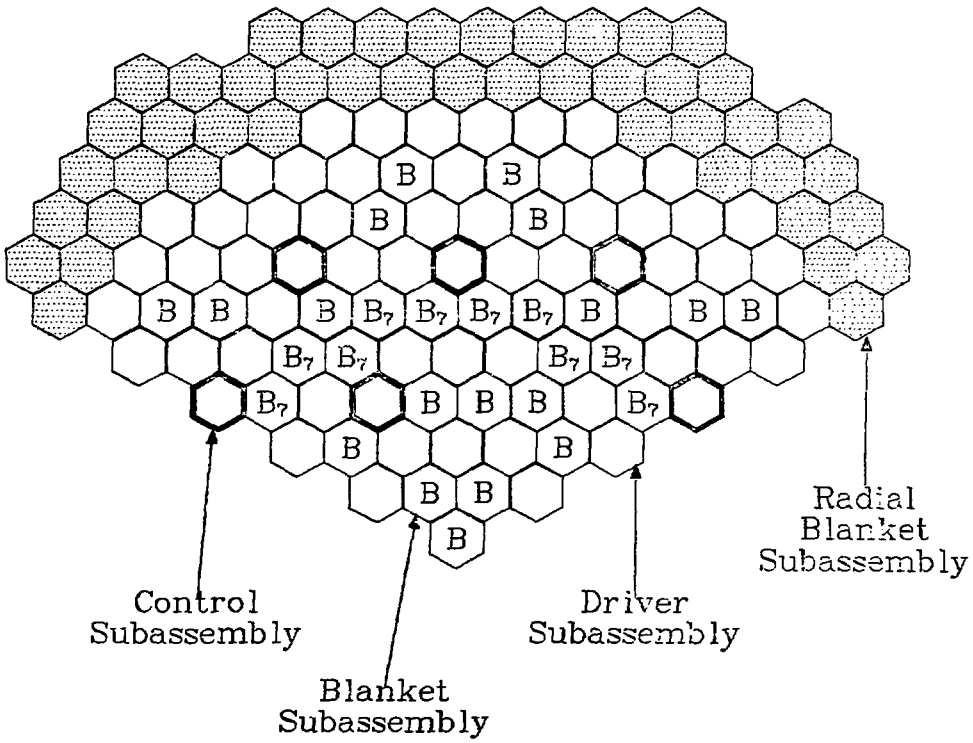

Fig. 1.
CRBR heterogeneous core.

A. Geometric Arrangement and SIMMER-II Mesh

The SIMMER-II cylindrical geometry used for these calculations is illustrated in Fig. 2. It consisted of a single blanket subassembly whose active core portion was surrounded by a disrupted pool region. The cross-sectional area of the pool represented that of six neighboring subassemblies and was bounded above and below by rigid structure. The subassembly wall separated the sodium-filled pin bundle from its radial surroundings.

The calculational mesh had five radial cells or rings (I = 1,..,5) and thirty-one axial cells (J = 1,..,31). The inner three rings representing the blanket subassembly had equal areas as did the outer two rings that represented the pool. The inner three rings, superimposed on a blanket subassembly containing 61 pins, are illustrated in Fig. 3. The axial noding is indicated in Fig. 2. Axially, the blanket subassembly consisted of an upper reflector (UR), a fission gas plenum (FGP), an upper axial blanket (UAB), an active core, a lower axial blanket (LAB), and a lower reflector (LR). The active core with nine axial cells 0.1016 m in height and the axial blankets were assumed to have identical material composition for this investigation and are delineated only to show the alignment with the pool formed from neighboring molten driver core material.

With this noding the single subassembly was treated as two-dimensional with r-z geometry. However, in some cases it was desirable to consider the subassembly as one dimensional. For those situations the inner three rings were combined into one with the outer two rings remaining unchanged.

B. Initial and Boundary Conditions

A whole core calculation of an HCDA was performed recently for the heterogeneous CRBR reactor * SAS3D was used to calculate the initiating phase of the accident. For initial conditions we used the coolant, cladding, blanket pellets, and subassembly wall axial temperature profiles for Ring 7 (as denoted by the blanket assemblies so marked in Fig. 1) at the end of the SAS3D calculation. In addition, the SAS3D calculation supplied corresponding top and bottom pressure boundary conditions of 0.1693 and 0.8116 MPa, respectively. This initial state is shown graphically in Fig. 4.

*This information was supplied by R. J. Bergeron, General Electric Company, May 1981.

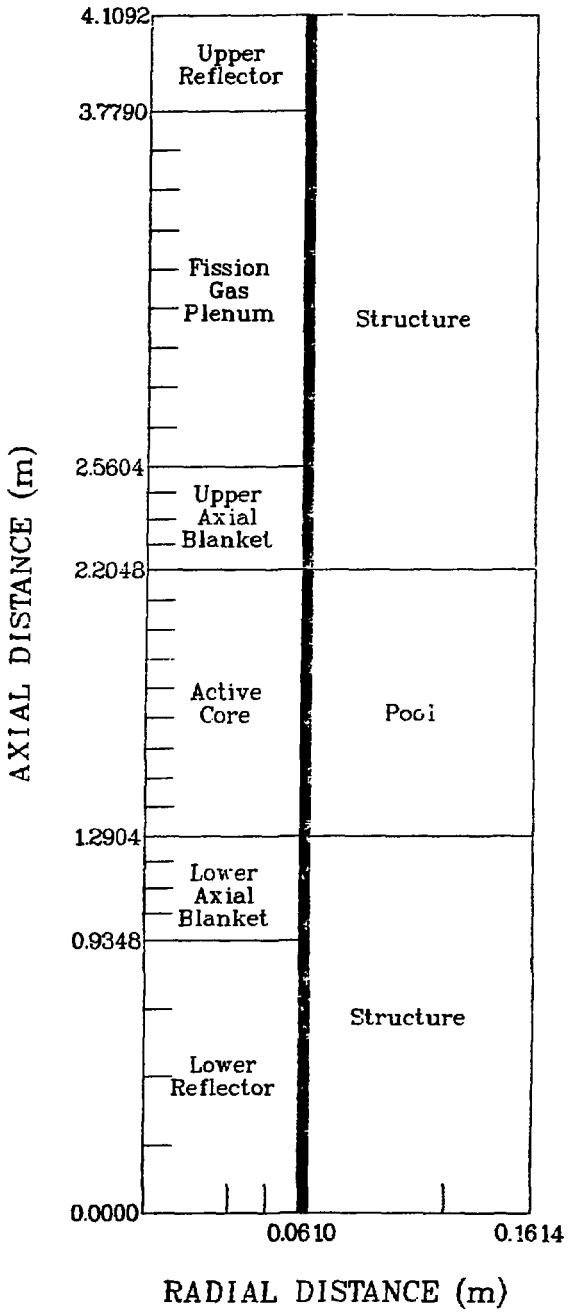

Fig. 2.
Geometrical representation of the blanket subassembly and its surroundings. Tic marks indicate the radial and axial meshes.

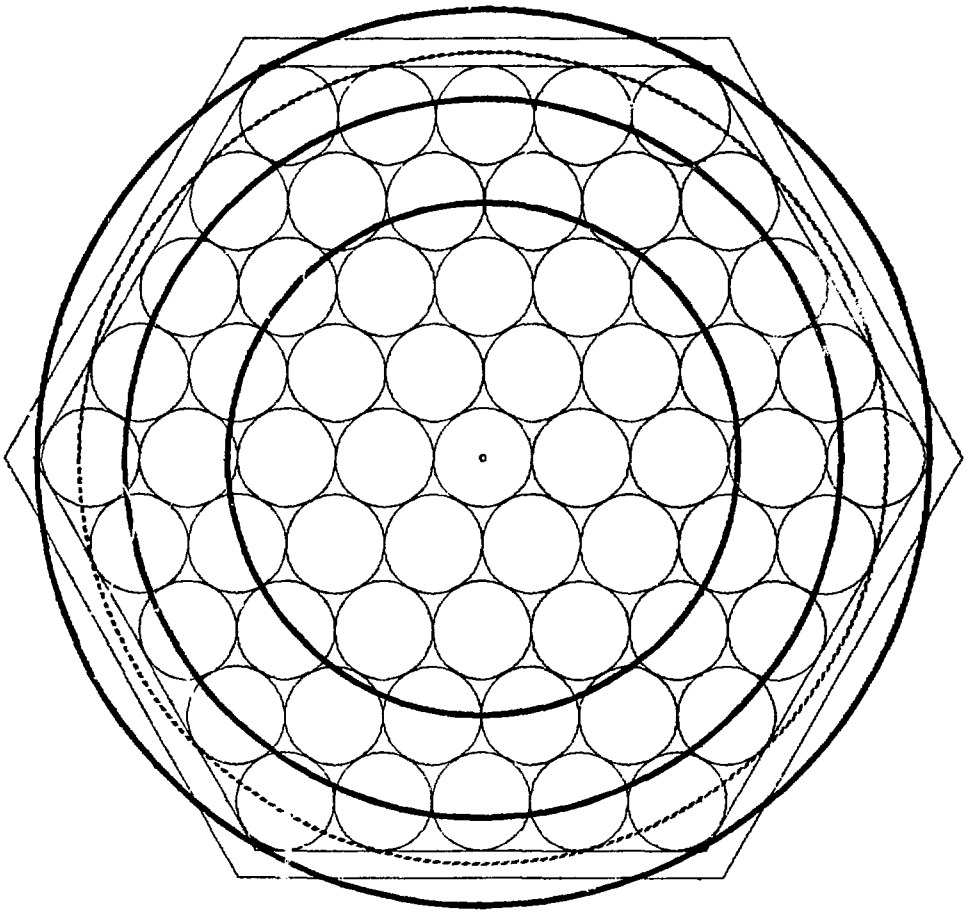

Fig. 3.
The SIMMER-II radial blanket mesh overlaid on the radial blanket CRBR subassembly. Dashed line indicates the inside subassembly wall.

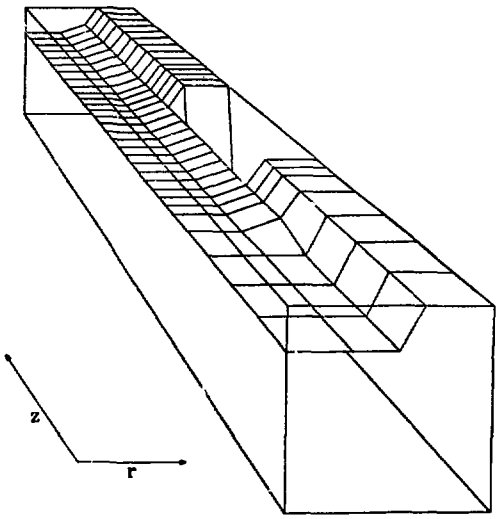

(a) Structure volume fraction.
(Min = 0., Max = 0.99)

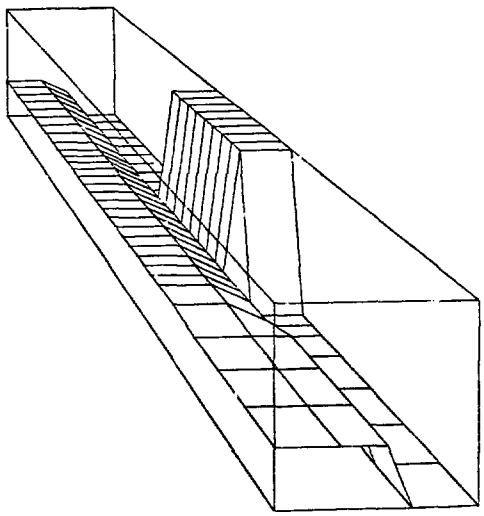

(b) Liquid volume fraction.
(Min = 0.01, Max = 0.70)

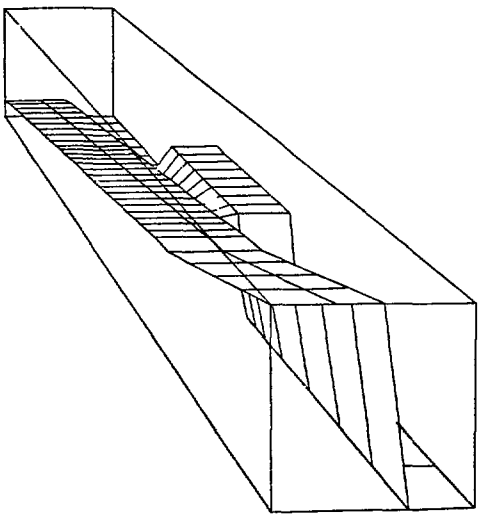

(c) Pressure (MPa)
(Min = 0.114, Max = 0.754)

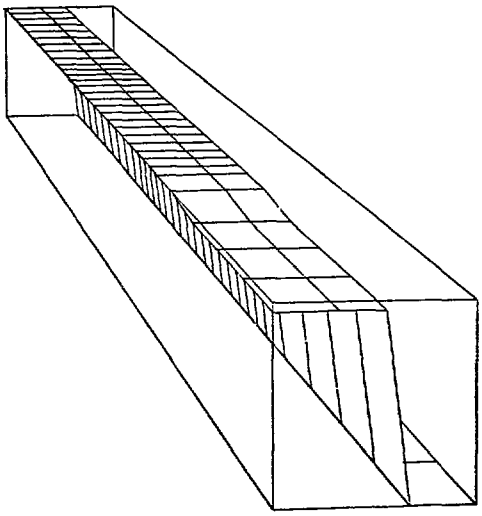

(d) Liquid axial velocity (m/s).
(Min = 0., Max = 5.66)

Fig. 4.
Initial state for the two-dimensional single subassembly and surroundings.

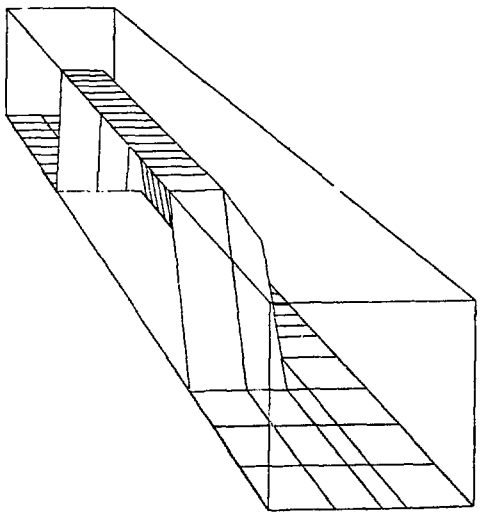

(e) Fabricated fertile fuel macroscopic density (kg/m^3). (Min = 0., Max = 5777.)

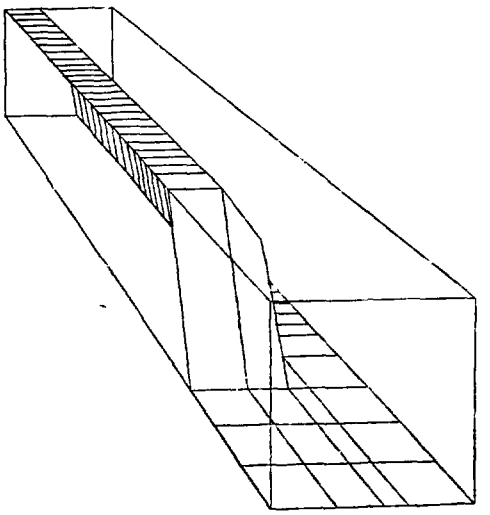

(f) Cladding macroscopic density (kg/m^3). (Min = 0., Max = 629.)

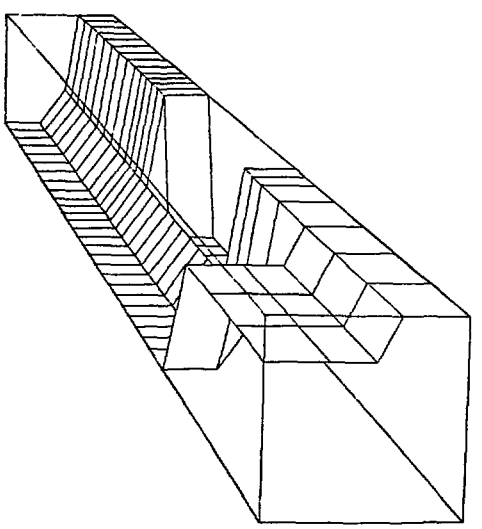

(g) Subassembly macroscopic density (kg/m^3). (Min = 0., Max = 7183.)

Fig. 4. (cont.)
Initial state for the two-dimensional single subassembly and surroundings.

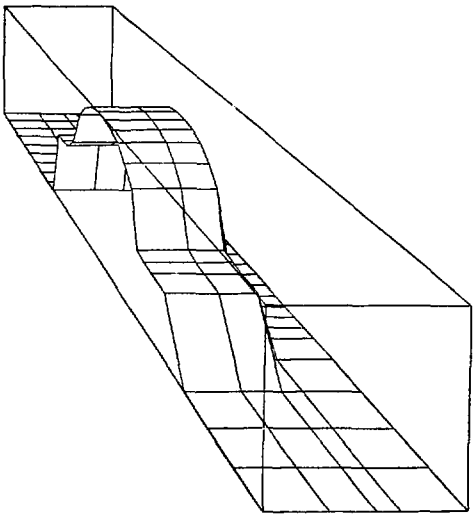

(h) Fabricated fuel temperature (K).
(M.n = 0., Max = 1784.)

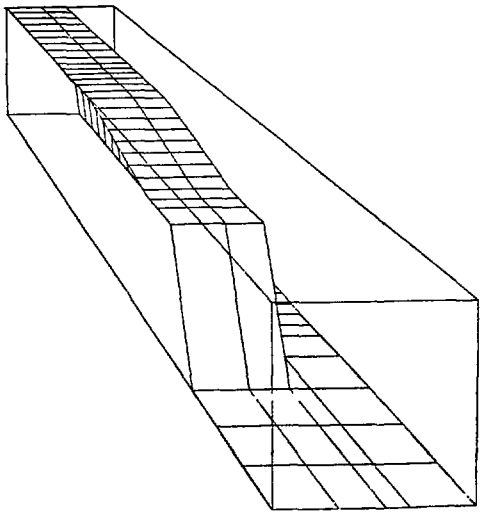

(i) Cladding temperature (K).
(Min = 0., Max = 837.)

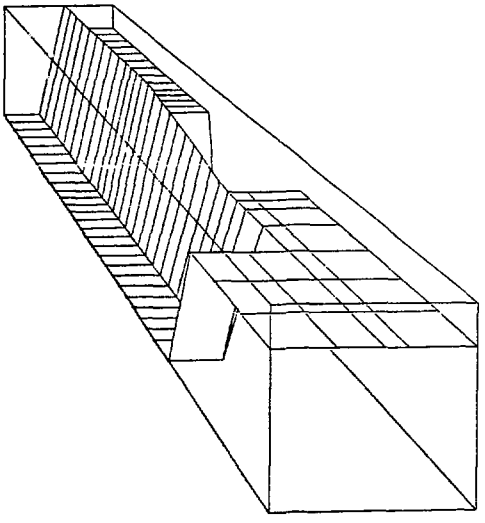

(j) Subassembly wall temperature (K).
(Min = 0., Max = 837.)

Fig. 4. (cont.)
Initial state for the two-dimensional single subassembly and surroundings.

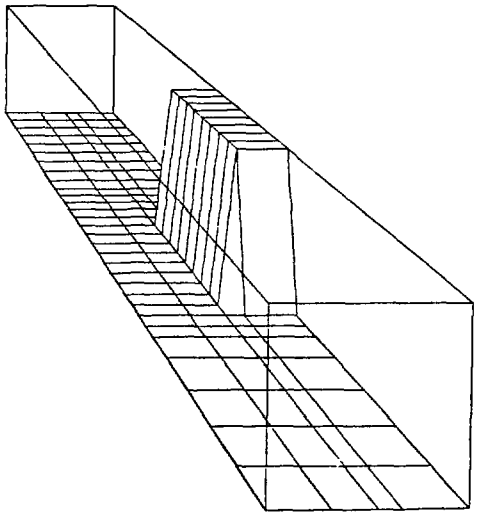

(k) Liquid fertile fuel macroscopic density (kg/m^3). (Min = 0., Max = 3484.)

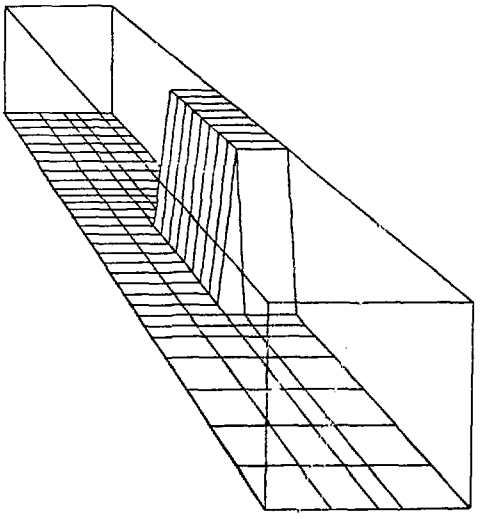

(l) Liquid fissile fuel macroscopic density (kg/m^3). (Min = 0., Max = 871.)

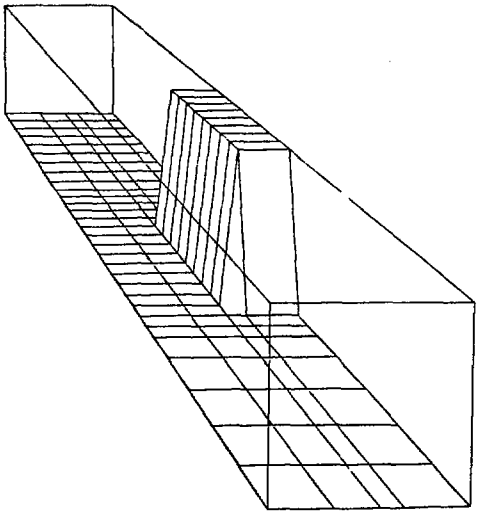

(m) Liquid steel macroscopic density (kg/m^3). (Min = 0., Max = 1358.)

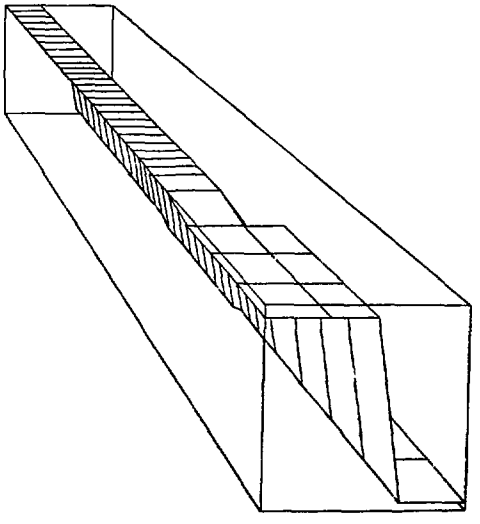

(n) Liquid sodium macroscopic density (kg/m^3). (Min = 0., Max = 189.)

Fig. 4. (cont.)
Initial state for the two-dimensional single subassembly and surroundings.

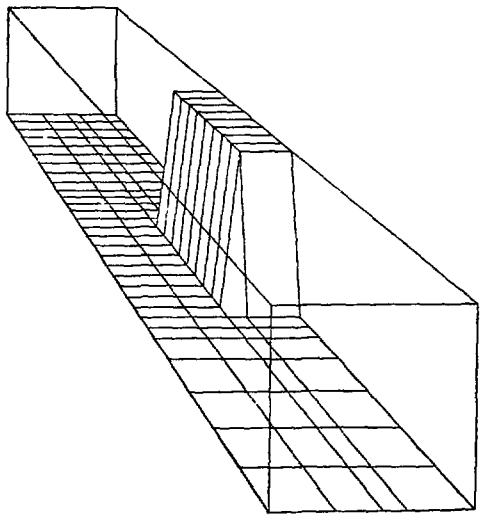

(o) Liquid fuel temperature (K).
(Min = 0., Max = 3200.)

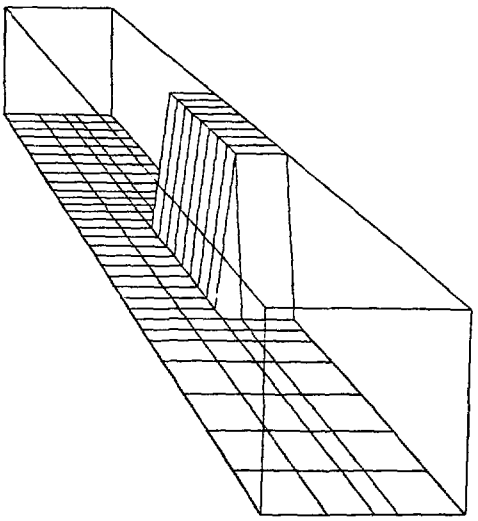

(p) Liquid steel temperature (K).
(Min = 0., Max = 3200.)

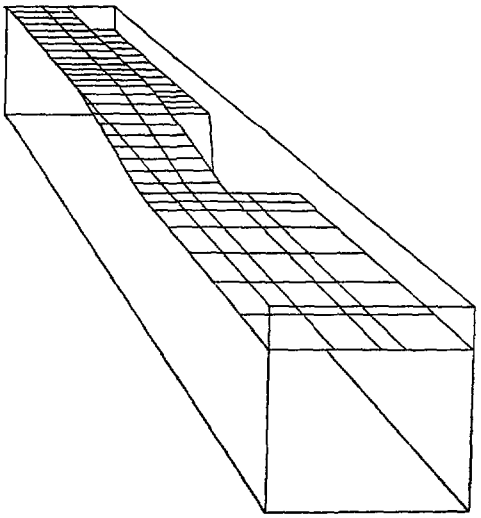

(q) Liquid sodium temperature (K).
(Min = 0., Max = 837.)

Fig 4. (cont.)
Initial state for the two-dimensional single subassembly and surroundings.

C. Subassembly Flow Initialization

Before allowing the single subassembly to interact with its surroundings by way of subassembly wall failure, a typical quasi-steady-state flow mode was established by using a previously determined value for the liquid-structure turbulent-flow friction-factor coefficient. In SIMMER-II this friction factor is of the form

$$f_{LS} = f_{LS1} Re_L^b \quad ,$$

where Re_L is the liquid Reynolds number, and b and f_{LS1} are input parameters. For this work b = -0.2 and f_{LS1} = 0.0939.[3] The input orifice coefficient at the inlet to the lower reflector was then adjusted to 7.3750 to give a mass flow characteristic of the end-of-initiation phase of an HCDA.

For our one-dimensional single subassembly with intact geometry, the liquid velocity would have one uniform value in the lower reflector and another through the remainder of the axial geometry together with uniform pressure gradients in these regions. For the two-dimensional subassembly we included internode shear viscosity in the SIMMER-II calculations. In addition, the intact geometry hydraulic diameter of Ring 3 was 60 percent of the hydraulic diameters of Rings 1 and 2 because the subassembly wall was included in Ring 3 (see Fig. 3). This modeling led to an axial flow with a nearly parabolic radial profile that was somewhat arbitrary because the hydraulic diameters depended on the choice of the cell sizes of the radial rings.

Sodium boiling was not allowed in the initial steady flow calculation because the availability of liquid sodium was an inherent part of this investigation. To prevent sodium boiling the maximum cladding and blanket pellet temperatures from the SAS3D results were reduced slightly (rather than eliminate structure-to-liquid heat transfer).

III. PARAMETRIC CASES CONSIDERED

We assumed for our parametric transient calculations that the system was in a quasi-steady state when the subassembly wall failed. The original intent was to determine analytically a steady state for each case considered and to use the resulting flow velocities and pressure profiles as input for the SIMMER-II transient calculation. It soon became evident that this was not

necessary for the parameter changes we were making. Starting with a base case already in steady-state flow, it took only a few time steps of SIMMER-II calculation to establish a new steady state for any changes in input parameters that we made. We induced subassembly wall failure in selected locations by inputting a subassembly wall thickness in such regions that was 0.2 of the nominal value and a heat-transfer coefficient reduced by an order of magnitude on the subassembly side. It then took only about 20-30 ms for wall failure and initiation of the transient (well after a steady state was established). Because SIMMER-II is a two-dimensional code with azimuthal symmetry we could model crack formation only in the sense that the subassembly wall was completely removed in one or more axial nodes.

The parameters varied in the calculations were (1) initial pool fuel temperature, (2) pool injection pressure, (3) subassembly wall opening size and location, (4) geometric modeling of the subassembly, (5) coolant driving pressure at the bottom of the subassembly, and (6) liquid-liquid heat-transfer multipliers. A total of 18 cases with various values of the above parameters is listed in Table I; Case 1 was chosen as the Base Case. Relative to the Base Case, Cases 2 and 3 had larger initial pool pressures. Cases 4 and 5 treated the subassembly one dimensionally (one radial ring) with Case 5 at a larger initial pool pressure. Cases 6, 7, and 8 had lower initial pool temperatures and the initial pool pressures varied from smaller to larger than the Base Case. In Cases 9, 10, and 11 the subassembly wall breaches were varied from smaller to larger than the Base Case. Cases 12, 13, 14 were run at lower pool temperatures and pressures but with wall opening location varying from the top to the bottom of the active core region. Cases 15 and 16 involved increasing the pressure at the bottom of the subassembly, and Cases 17 and 18 allowed the liquid-liquid heat transfer to be greater than and less than that of the Base Case, respectively.

IV. ANALYSIS AND CASE COMPARISONS

A. Analysis of Base Case

Case 1, chosen to be the Base Case, represented a two-dimensional SIMMER-II calculation of the response of an internal blanket subassembly to a surrounding pool of molten fuel and steel at 4800 K and at a pressure of 3.02 MPa. The subassembly wall in a cell at the midplane of the active core (I = 3, J = 13) was subjected to melting attack and failure, permitting the

TABLE I

PARAMETERS USED FOR THE EIGHTEEN CALCULATED CASES

Case	Initial Pool Fuel Temp (K)	Initial Pool Pressure (MPa)	Wall Opening[a]	Subassembly Dimension	Bottom Pressure (MPa)	Liquid-liquid Heat-Transfer Multipliers
1	4800	3.02	1.	2	0.3	1.
2	4800	6.00	1.	2	0.3	1.
3	4800	9.00	1.	2	0.3	1.
4	4800	3.02	1.	1	0.3	1.
5	4800	9.00	1.	1	0.3	1.
6	3200	0.50	1.	2	0.3	1.
7	3200	3.02	1.	2	0.3	1.
8	3200	6.00	1.	2	0.3	1.
9	4800	3.02	0.250	2	0.3	1.
10	4800	3.02	0.0625	2	0.3	1.
11	4800	3.02	9.	2	0.3	1.
12	4000	0.35	1.	2	0.3	1.
13	4000	0.35	1.(J = 17)	2	0.3	1.
14	4000	0.35	1.(J = 9)	2	0.3	1.
15	4000	0.35	1.	2	3.0	1.
16	4800	6.00	1.	2	3.0	1.
17	4800	3.02	1.	2	0.3	5.
18	4800	3.02	1.	2	0.3	0.1

[a]Fraction of Base Case opening area.

high-temperature and -pressure molten fuel-steel mixture to interact with the relatively cool sodium flowing in the subassembly. The wall failed at t = 0.024 s because of the initially thin wall at the desired failure location (Fig. 5a) with the ensuing fuel-coolant interaction producing sodium vapor at a pressure of 4.66 MPa (Fig. 5c). The opening had an area of 0.0389 m^2 or $(7.77\ in)^2$. (See Appendix A for an estimation of the maximum crack opening area for a hexagonal duct failed at one corner.) Some of the sodium vapor produced initially flowed into the pool region causing considerable pool material to move to the axial extremities of the pool (Fig. 5b, d, e). The liquid sodium was completely removed from node J = 13 of the subassembly (Fig. 5f), and the pressure caused liquid sodium above the middle of the core to begin to move upward and that below the middle of the core to move downward with velocities of the order of 100 m/s (Fig. 5g).

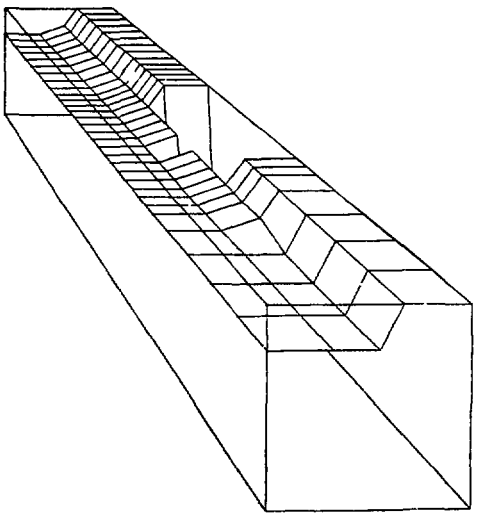

(a) Structure volume fraction. (Min = 0., Max = 0.99.)

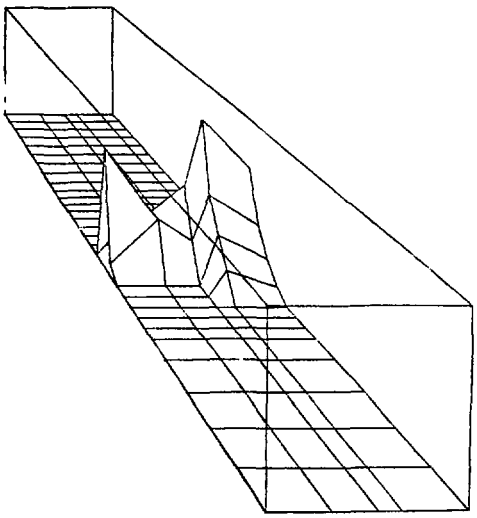

(b) Sodium vapor macroscopic density (kg/m^3). (Min = 0., Max = 3.39.)

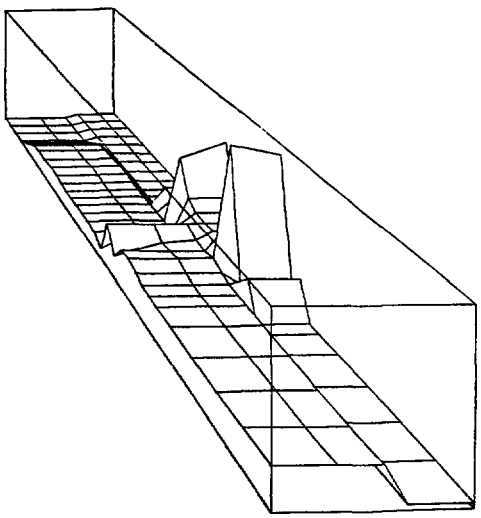

(c) Pressure (MPa). (Min = 0.05, Max = 15.44.)

Fig. 5.
Case 1 variables at 0.03 s.

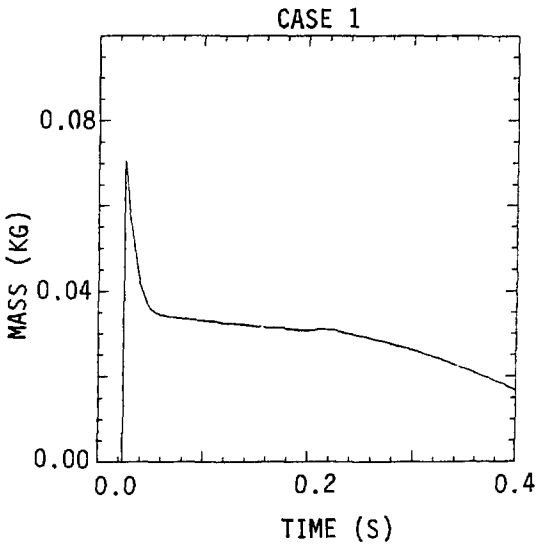

(d) Sodium vapor mass in pool.

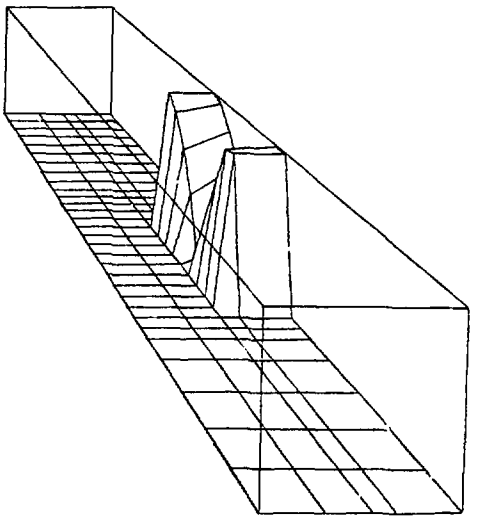

(e) Liquid fissile fuel macroscopic density (kg/m^3). (Min = 0., Max = 1177.)

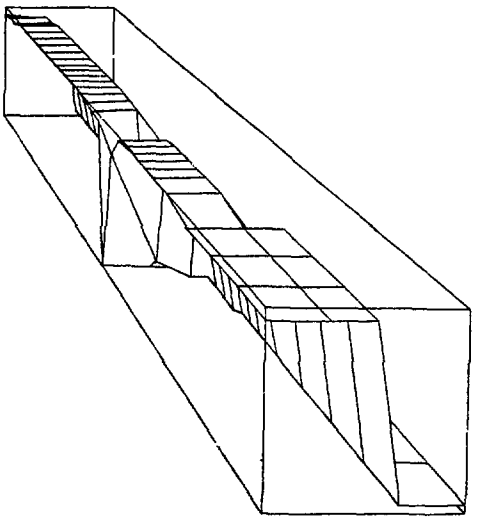

(f) Liquid sodium macroscopic density (kg/m^3). (Min = 0., Max = 190.)

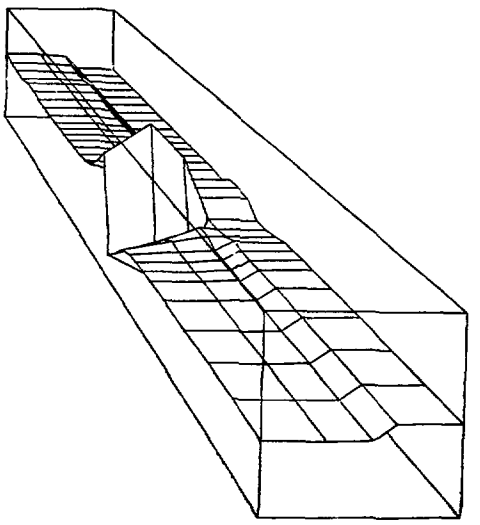

(g) Liquid axial velocity (m/s). (Min = -96.6, Max = 115.6)

Fig. 5. (cont.)
Case 1 variables at 0.03 s.

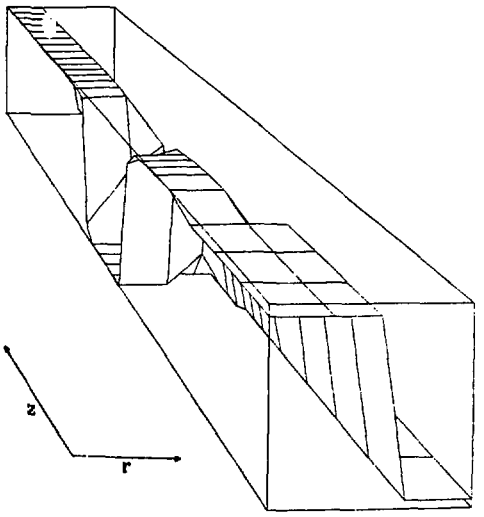

(a) Liquid sodium macroscopic density (kg/m^3). (Min = 0., Max = 190.)

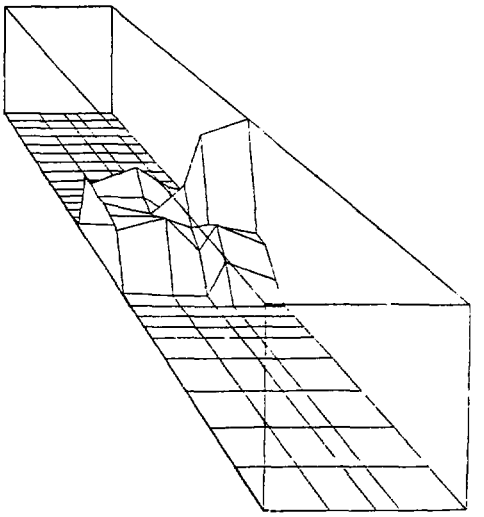

(b) Sodium vapor macroscopic density (kg/m^3). (Min = 0., Max = 2.32)

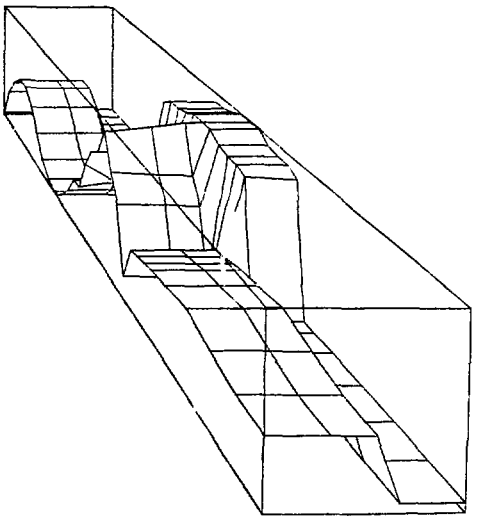

(c) Pressure (MPa). (Min = 0.26, Max = 4.93)

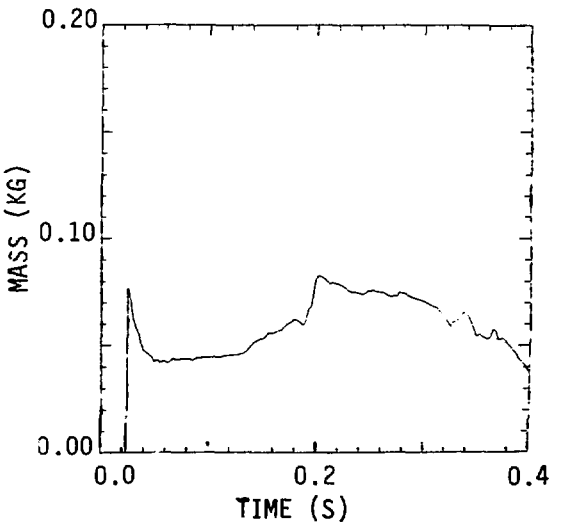

(d) Sodium vapor mass in subassembly.

Fig. 6.
Case 1 variable at 0.04 s.

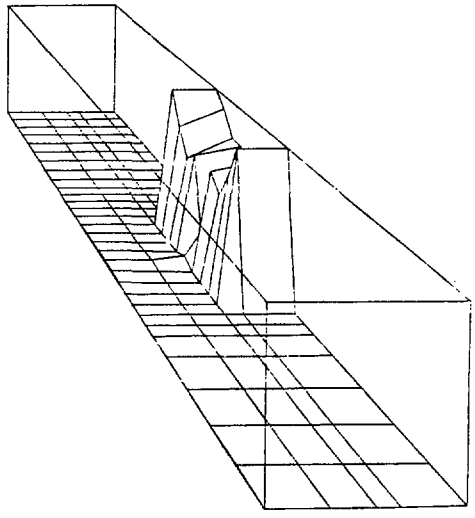

(e) Liquid fissile fuel macroscopic density (kg/m^3). (Min = 0., Max = 1182.)

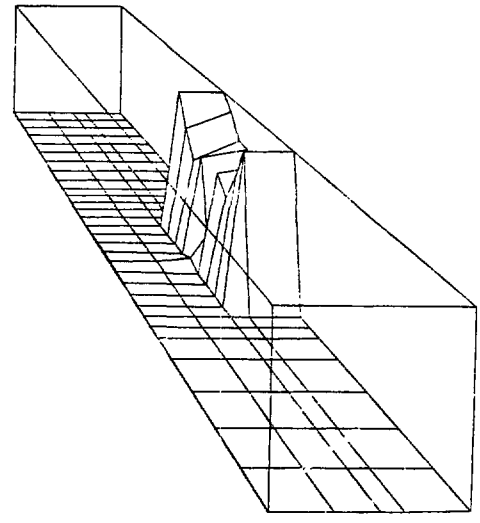

(f) Liquid steel macroscopic density (kg/m^3). (Min = 0., Max = 1844.)

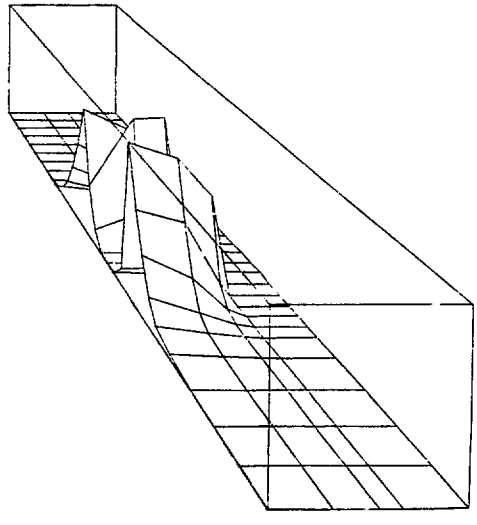

(g) Fissile fuel particle macroscopic density (kg/m^3) (Min = 0., Max = 15.15)

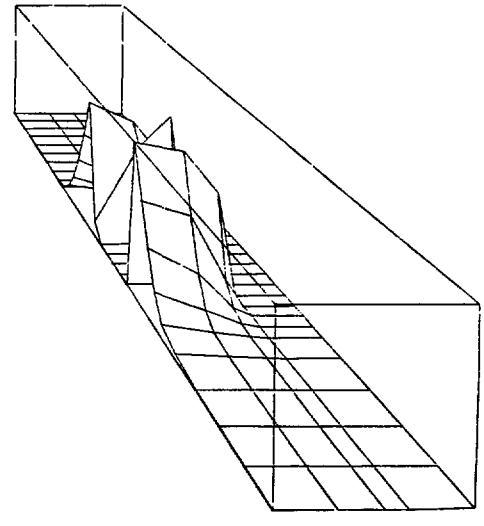

(h) Steel particle macroscopic density (kg/m^3). (Min = 0., Max = 17.21)

Fig. 6. (cont.)
Case 1 variable at 0.04 s.

By t = 0.04 s about half the active core had been voided of liquid sodium (Fig. 6a, b), although some lagged behind in Ring 3 (which contained the subassembly wall) because of wall drag effects (smaller liquid velocities) and the condensation of sodium vapor. Sodium vapor was condensing also near the active core extremities as was evidenced by the very low pressures there and by the decrease in total sodium vapor at that time (Fig. 6c, d). The molten fuel/steel still was localized mainly at the wall failure region in the subassembly (Fig. 6e, f). Fuel and steel particles had formed near the sodium liquid-vapor interface because of quenching of the molten mixture by liquid sodium and by the cold pins (Fig. 6g, h).

At 0.05 s cladding had started to melt at J = 13 (Fig. 7), and by 0.13 s it had failed in Rings 1 and 2 up to the fission gas plenum (Fig. 8). The pressure was high and nearly uniform up to the FGP and then decreased rapidly at the upper liquid sodium interface to the low pressure boundary at the top of the upper reflector. The upper liquid sodium interface for Rings 1 and 2 had progressed three nodes into the FGP (which contained cladding but no fuel pellets). By 0.14 s cladding had failed in Ring 1 of the first axial node (J = 22) of the FGP, depleting this cell of structure (Fig. 9). Liquid sodium in Ring 3 then flashed as it moved radially into this low pressure cell forming a 65% void fraction there. The fuel blowdown continued to drive sodium out of the top of the assembly. More cladding melted and liquid fuel flashed as it entered the FGP (Fig. 10).

Subassembly walls were beginning to fail above the center of the active core by 0.370 s (Fig. 11). Cladding had failed throughout the subassembly except for Ring 3 above the UAB. Similarly liquid sodium had been expelled or vaporized except for Ring 3 above the UAB.

By 0.600 s the FGP and UR were completely voided and the pressure had been relieved in this portion of the subassembly (Fig. 12). The subassembly wall had failed throughout the active core; cladding had been completely removed; and liquid sodium no longer existed in the subassembly. Fuel and steel particles had been swept from the subassembly. The FGP and UR consisted, except for intact subassembly walls, of fuel and steel vapor. Liquid fuel and steel were still vaporizing as they flowed into the FGP, but the pressure in this region had been relieved by the high flow rates that developed because of the complete destruction of the pin structure. The fuel columns in the active core, UAB, and LAB were assumed to remain intact.

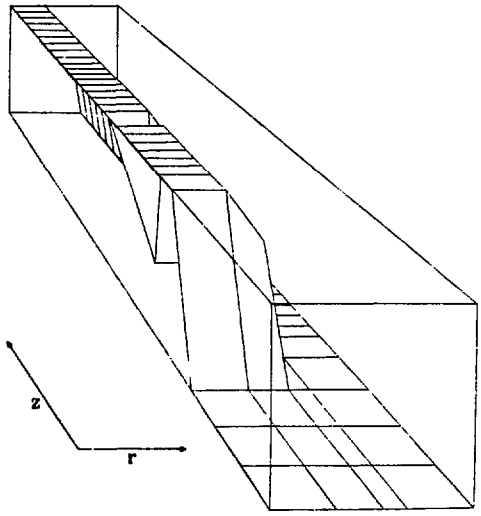

(a) Cladding macroscopic density (kg/m^3). (Min = 0., Max = 632.)

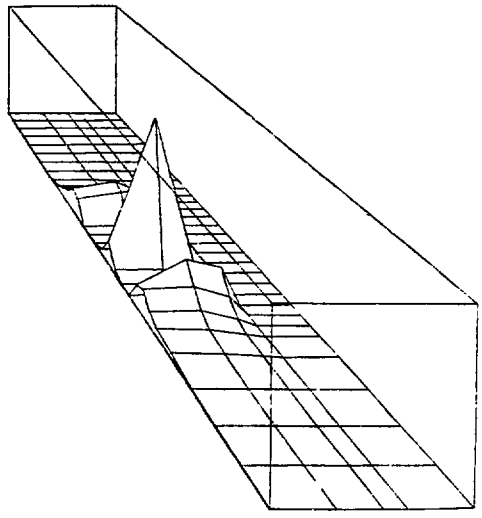

(b) Steel particle macroscopic density (kg/m^3). (Min = 0., Max = 121.)

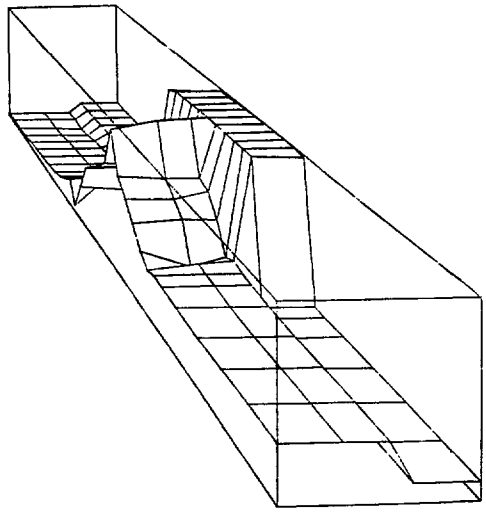

(c) Pressure (MPa). (Min = 0.06, Max = 4.58)

Fig. 7.
Case 1 variables at 0.05 s.

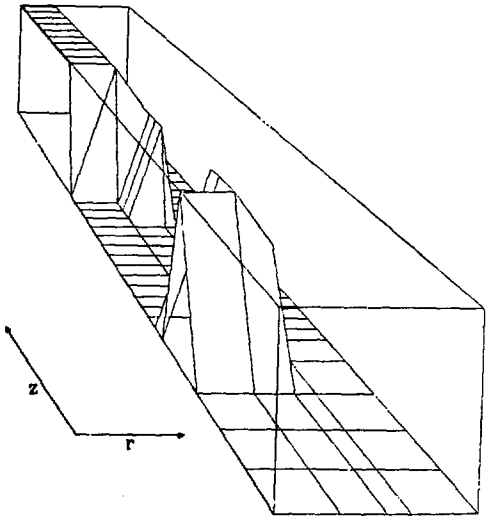

(a) Cladding macroscopic density (kg/m^3). (Min = 0., Max = 634.)

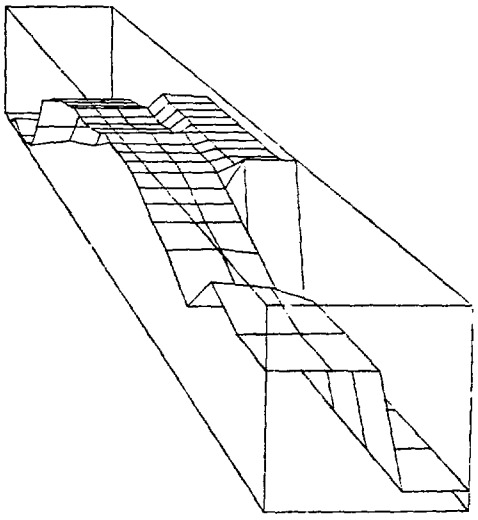

(b) Pressure (MPa). (Min = 0.06, Max = 4.65)

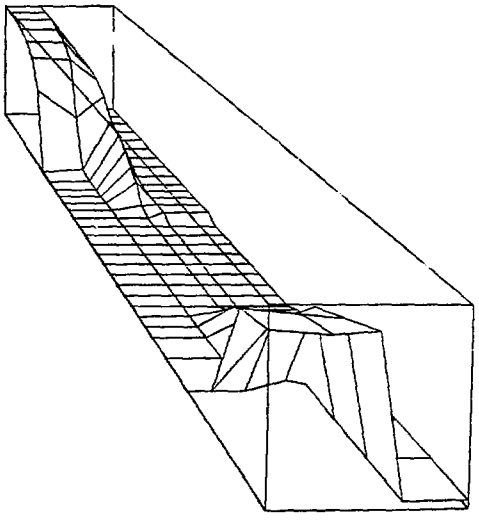

(c) Liquid sodium macroscopic density (kg/m^3). (Min = 0., Max = 187.)

Fig. 8.
Case 1 variables at 0.13 s.

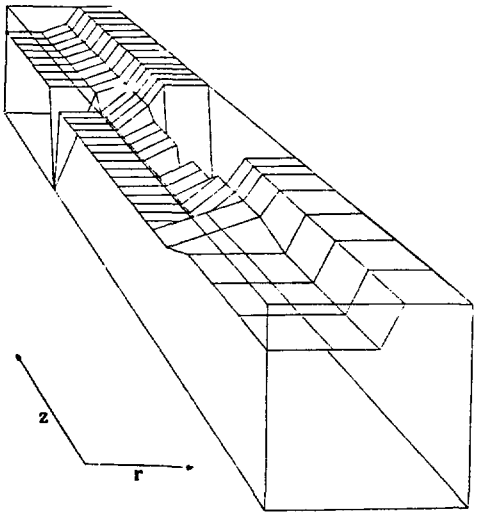

(a) Structure volume fraction. (Min = 0., Max = 0.99)

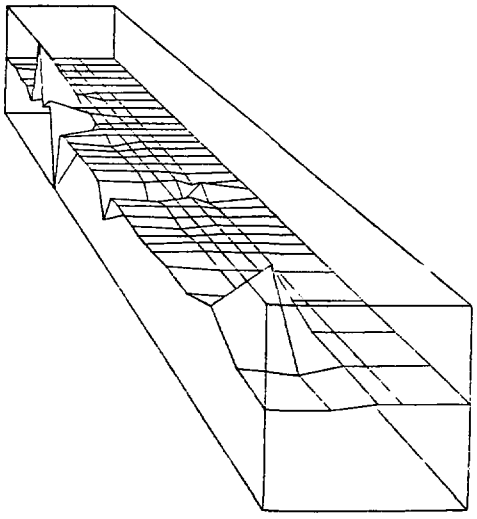

(b) Liquid radial velocity (m/s). (Min = -5.64, Max = 5.26)

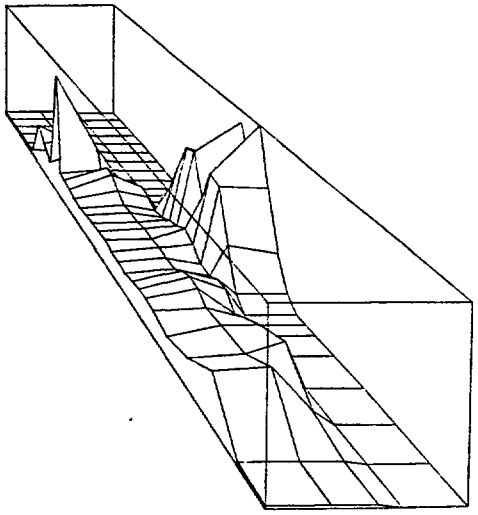

(c) Vapor volume fraction. (Min = 0., Max = 0.71)

Fig. 9.
Case 1 variables at 0.14 s.

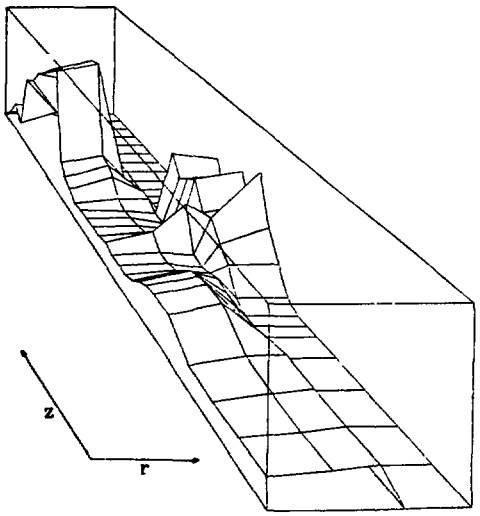

(a) Vapor volume fraction. (Min = 0., Max = 0.98)

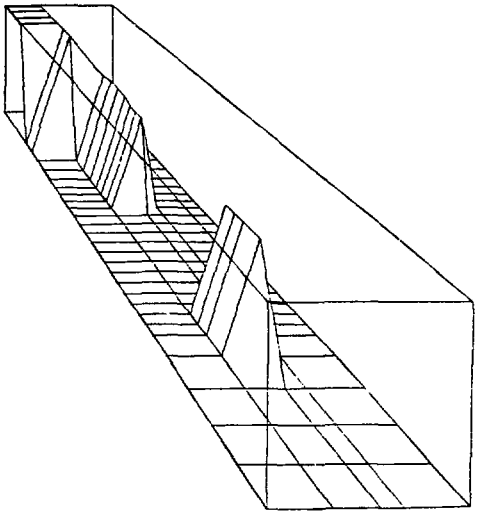

(b) Cladding macroscopic density (kg/m^3). (Min = 0., Max = 636.)

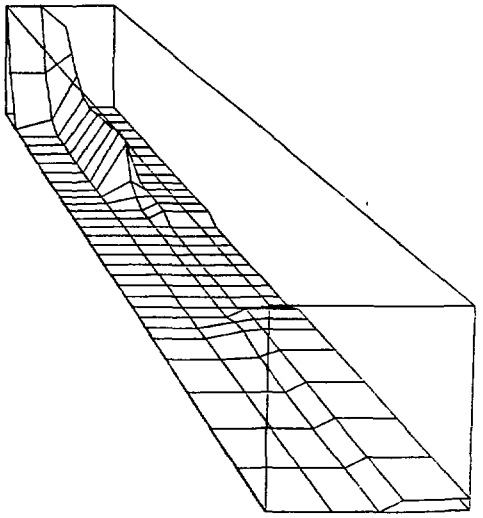

(c) Liquid sodium macroscopic density (kg/m^3). (Min = 0., Max = 136.)

Fig. 10.
Case 1 variables at 0.23 s.

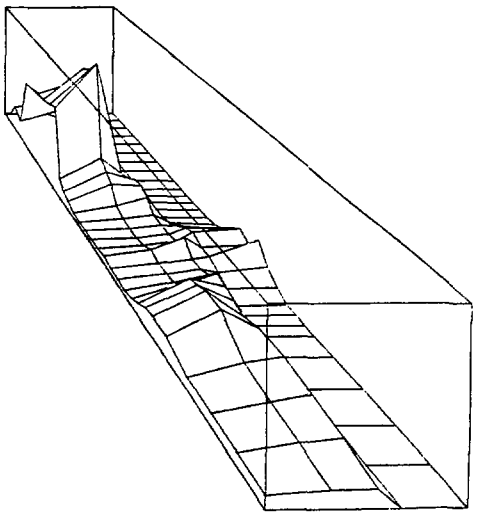

(d) Sodium vapor macroscopic density (kg/m^3). (Min = 0., Max = 5.76)

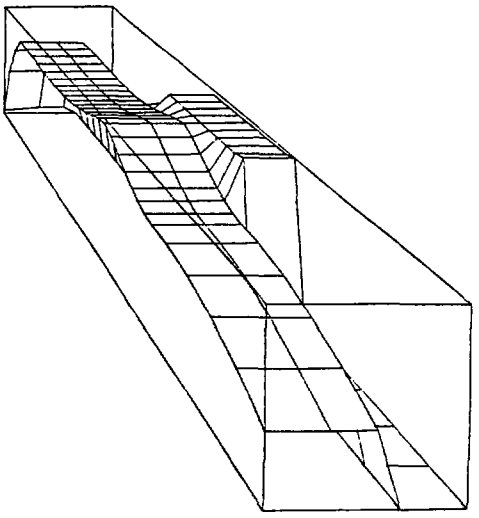

(e) Pressure (MPa). (Min = 0.5, Max = 5.0)

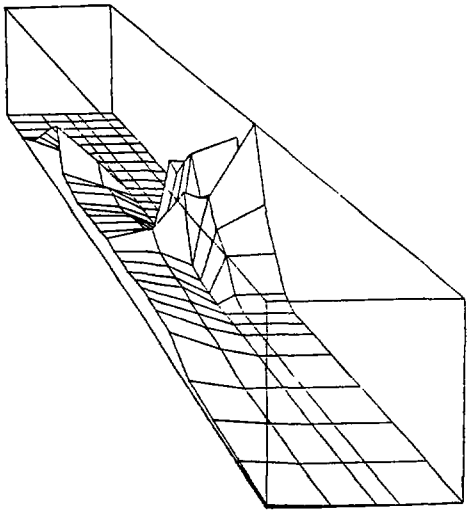

(f) Fuel vapor macroscopic density (kg/m^3). (Min = 0., Max = 7.12)

Fig. 10. (cont.)
Case 1 variables at 0.23 s.

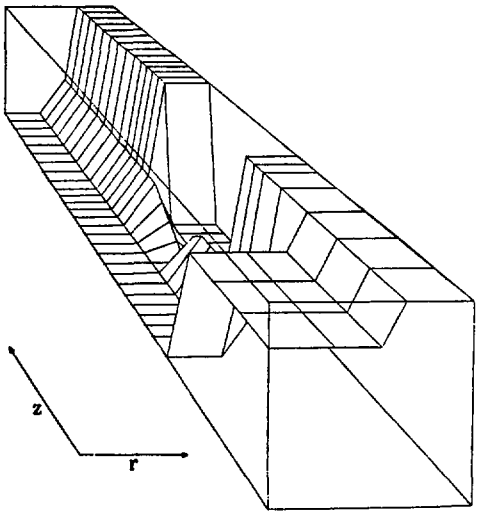

(a) Subassembly wall macroscopic density (kg/m^3) (Min = 0., Max = 7183.)

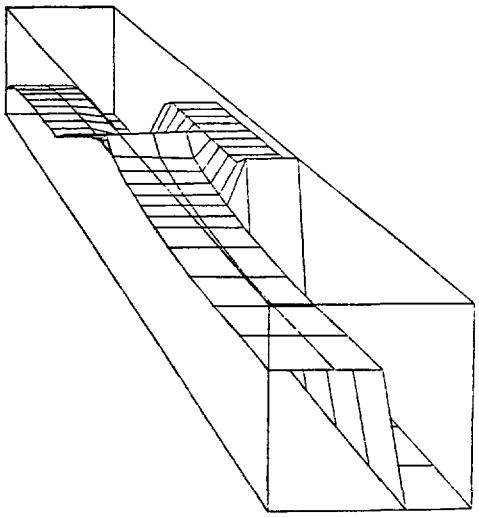

(b) Pressure (MPa) (Min = 0.5, Max = 5.34)

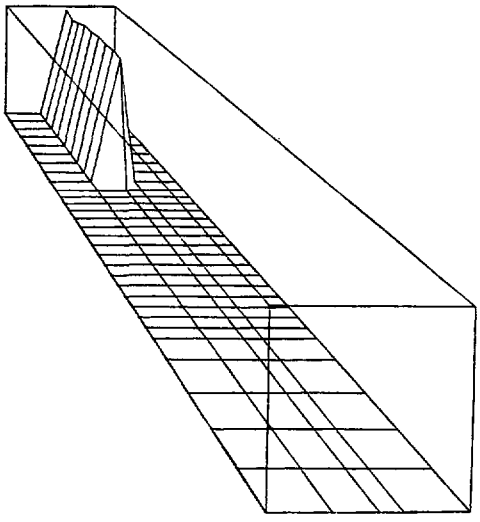

(c) Cladding macroscopic density (kg/m^3). (Min = 0., Max = 478.)

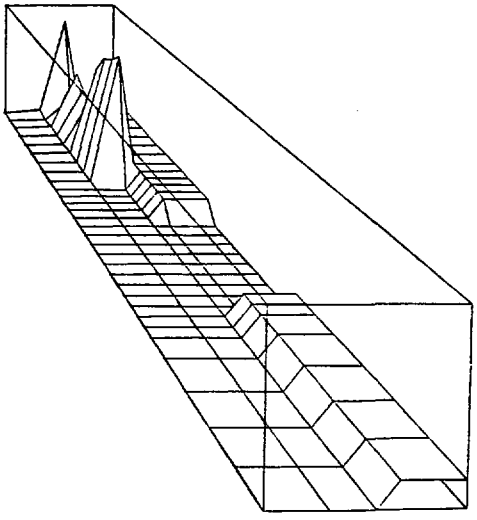

(d) Liquid sodium macroscopic density (kg/m^3). (Min = 0., Max 53.9)

Fig. 11.
Case 1 variables at 0.37 s.

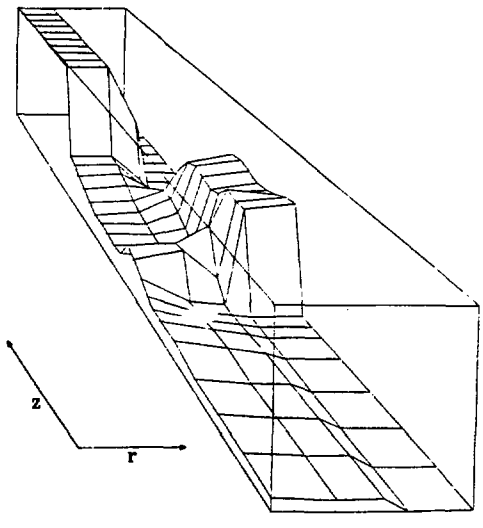

(a) Vapor volume fraction. (Min = 0., Max = 1.)

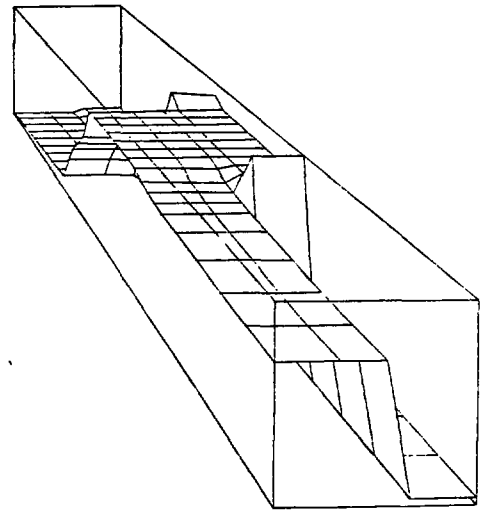

(b) Pressure (MPa) (Min = 0.3, Max = 5.2)

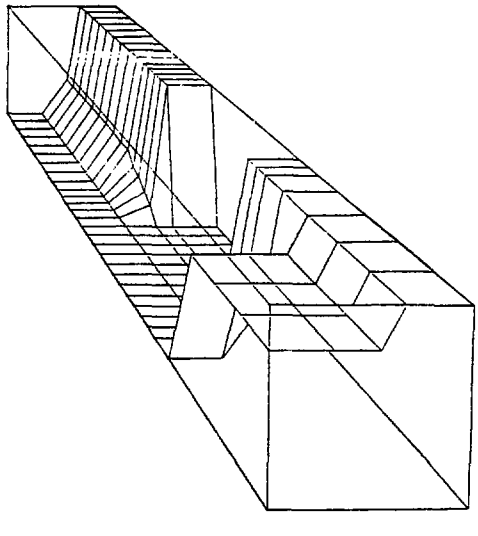

(c) Subassembly wall macroscopic density (kg/m^3). (Min = 0., Max = 7183.)

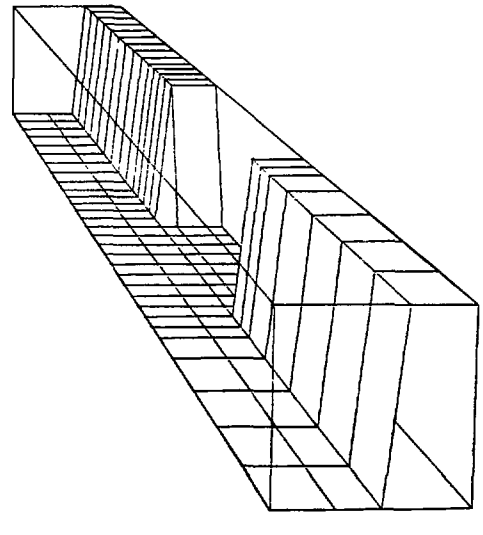

(d) Liquid sodium macroscopic density (kg/m^3). (Min = 0., Max = 7.71)

Fig. 12.
Case 1 variables at 0.60 s.

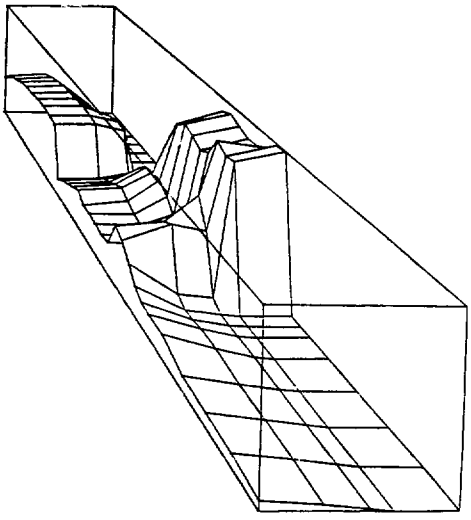

(e) Fuel vapor macroscopic density (kg/m^3). (Min = 0., Max = 4.08)

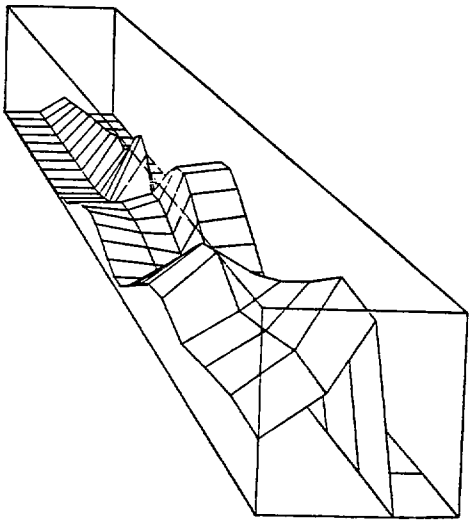

(f) Sodium vapor macroscopic density (kg/m^3). (Min = 0., Max = 0.21)

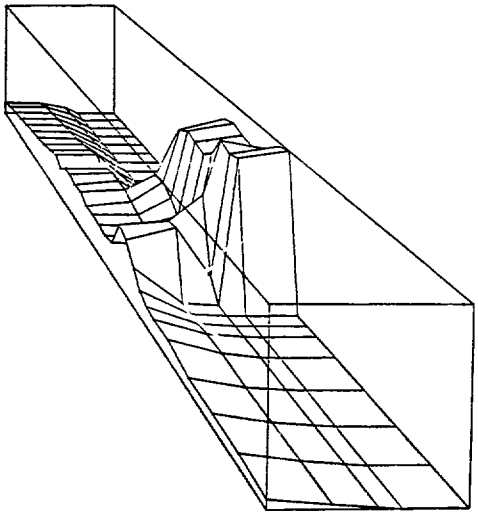

(g) Steel vapor macroscopic density (kg/m^3). (Min = 0., Max = 4.62)

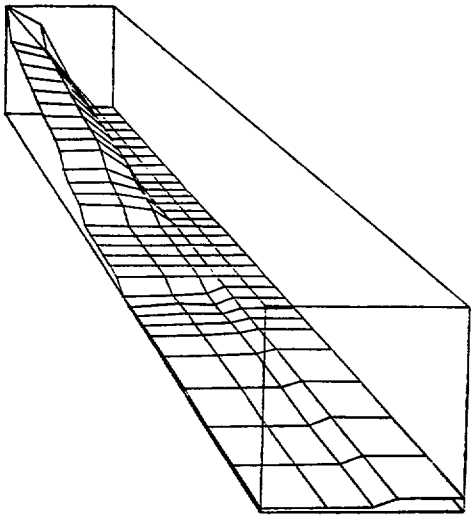

(h) Liquid axial velocity (m/s). (Min = -11.7, Max = 171.)

Fig. 12. (cont.)
Case 1 variables at 0.60 s.

B. Parameter Studies

In the preceding section the Base Case, Case 1, was examined in some detail. Here we compare the results of this Base Case and seventeen additional cases; the latter contain variations of certain parameters, as tabulated in Table I.

1. Pressure Pulses. In each case, shortly after the beginning of the calculation (t = 0.0 s) the blanket subassembly wall failed; this usually took a few tens of milliseconds. Hot molten fuel-steel pool material then came in contact with relatively cold flowing sodium within the subassembly causing a rapid pressure rise or, in a few cases, several maxima, as seen in Fig. 13. These pressures ranged from 2.6 MPa to 26 MPa. The highest pressures corresponded to: (1) Cases 3 and 5, which had high injection pressures; (2) Case 11 in which the subassembly wall throughout the whole active core region was allowed to fail instantly; and (3) Case 18 where decreased liquid-liquid heat transfer decreased the fuel/steel-coolant interaction rate and allowed more molten fuel mixing in the subassembly before sodium vapor production. The initial interaction pressure caused sodium in the subassembly to flow axially away from the wall opening and pool material to rebound back into the pool away from the opening. In most cases, after the initial pressure pulse(s) the pressure relaxed to a steady value; this relaxed value apparently depended mainly on the temperature of the pool and the area of the wall opening and to a lesser extent on the pool pressure.

Case 10 had four initial pressure maxima. Because the crack opening was very small, the first peak was less than the pool pressure, and the corresponding material rebound was not as great as in the other cases; this resulted in several pressure pulses closely spaced in time.

Cases 17 and 18 show the effects of increasing and decreasing all the liquid-liquid heat-transfer rates by direct multipliers. Although both cases relaxed to nearly the same pressures, the peak value for Case 18 was about three times greater. Because of the lower heat transfer in Case 18, greater mixing took place prior to the formation of sodium vapor, so that sodium vapor production was greatly increased when it did occur.

Cases 15 and 16 correspond to Cases 2 and 12, respectively, except that in the former cases the input fluid pressure at the bottom of the subassembly was increased by a factor of 10 causing increased coolant flow velocities. This resulted in peak pressures in Cases 15 and 16 that were much less than in

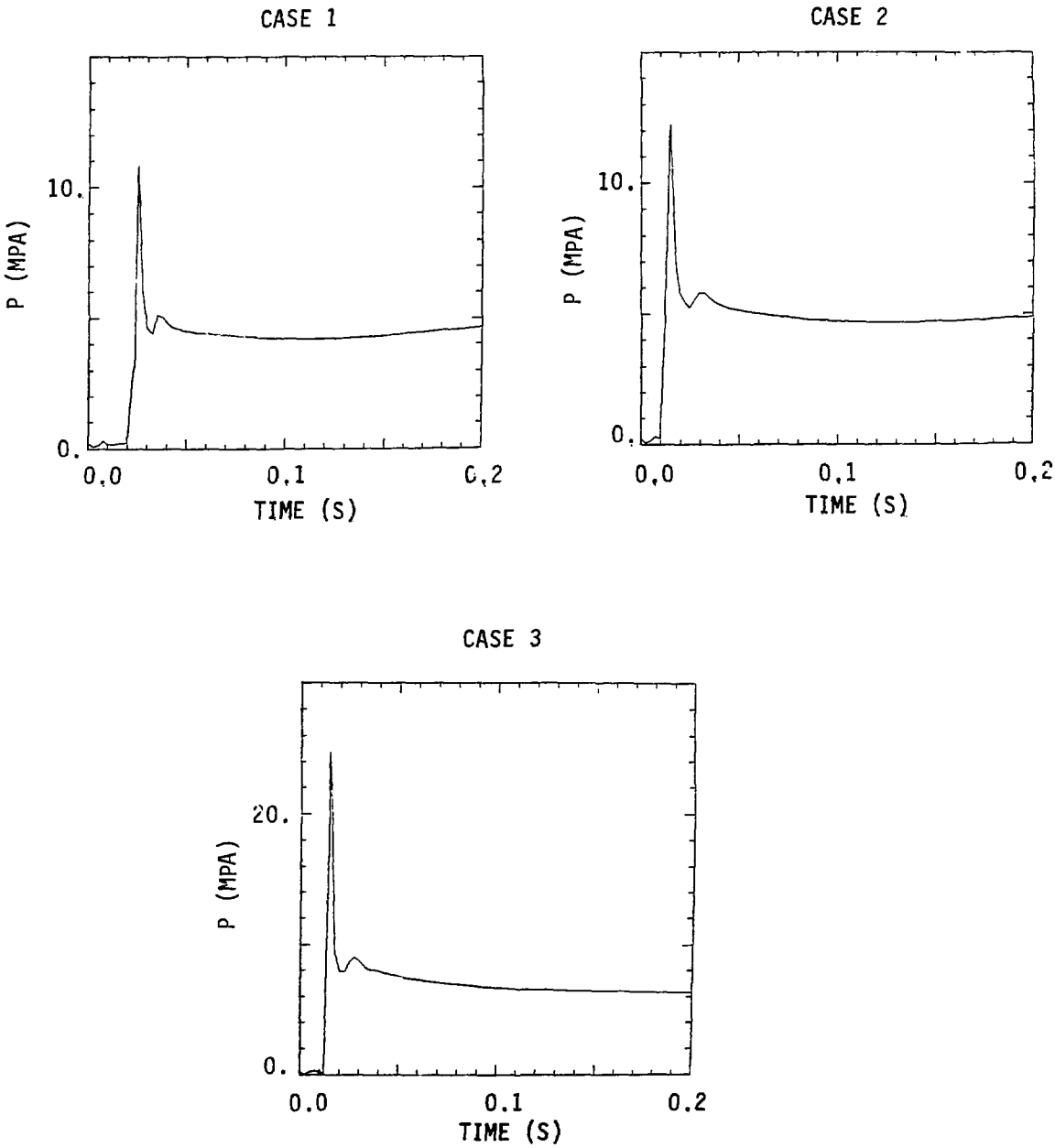

Fig. 13.
Blanket-subassembly midplane pressure vs time for each case.

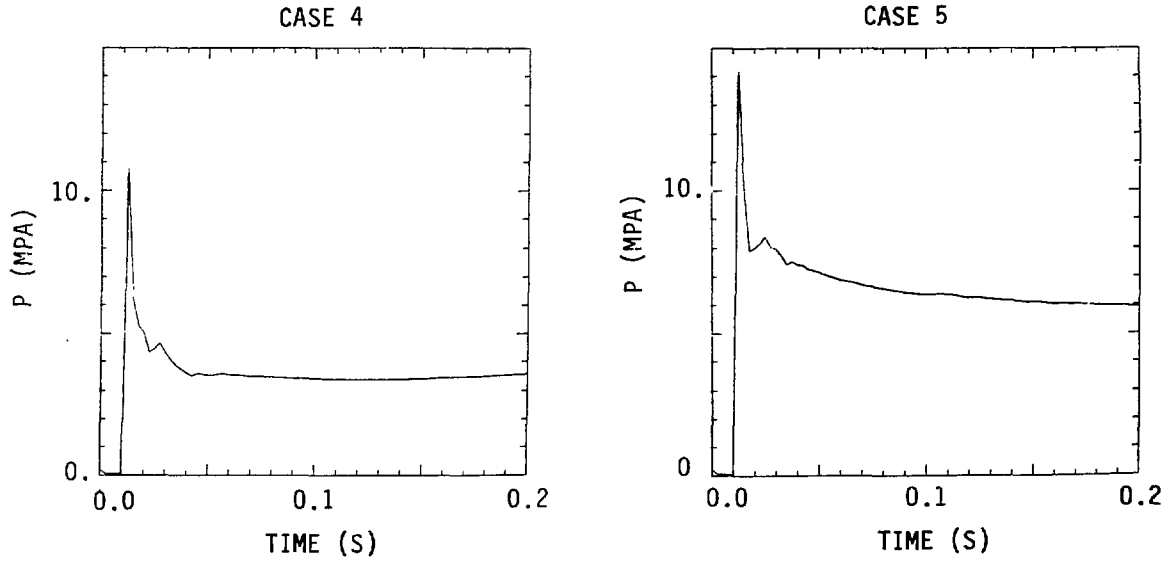

Fig. 13. (cont.)
Blanket-subassembly midplane pressure vs time for each case.

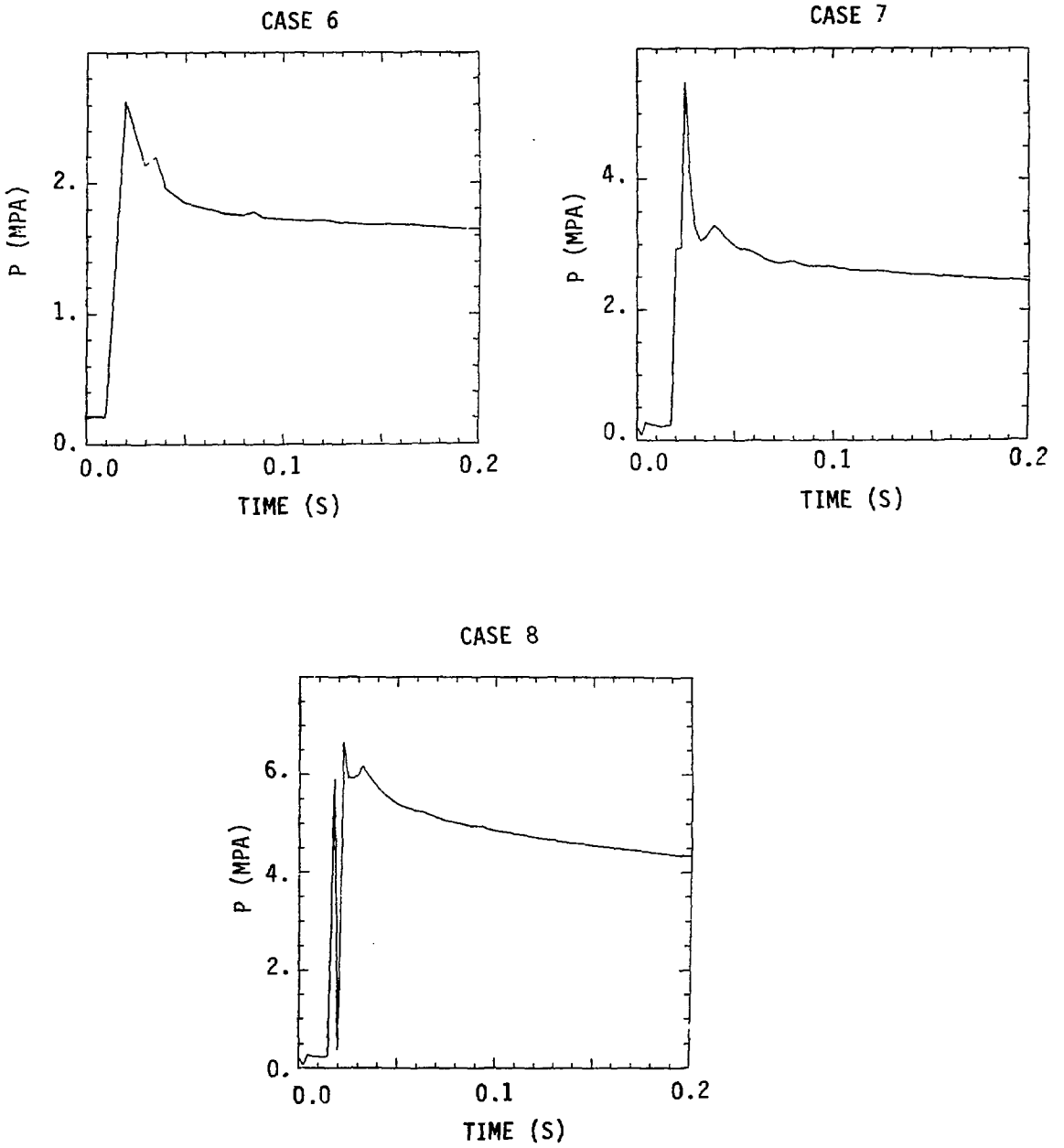

Fig. 13. (cont.)
Blanket-subassembly midplane pressure vs time for each case.

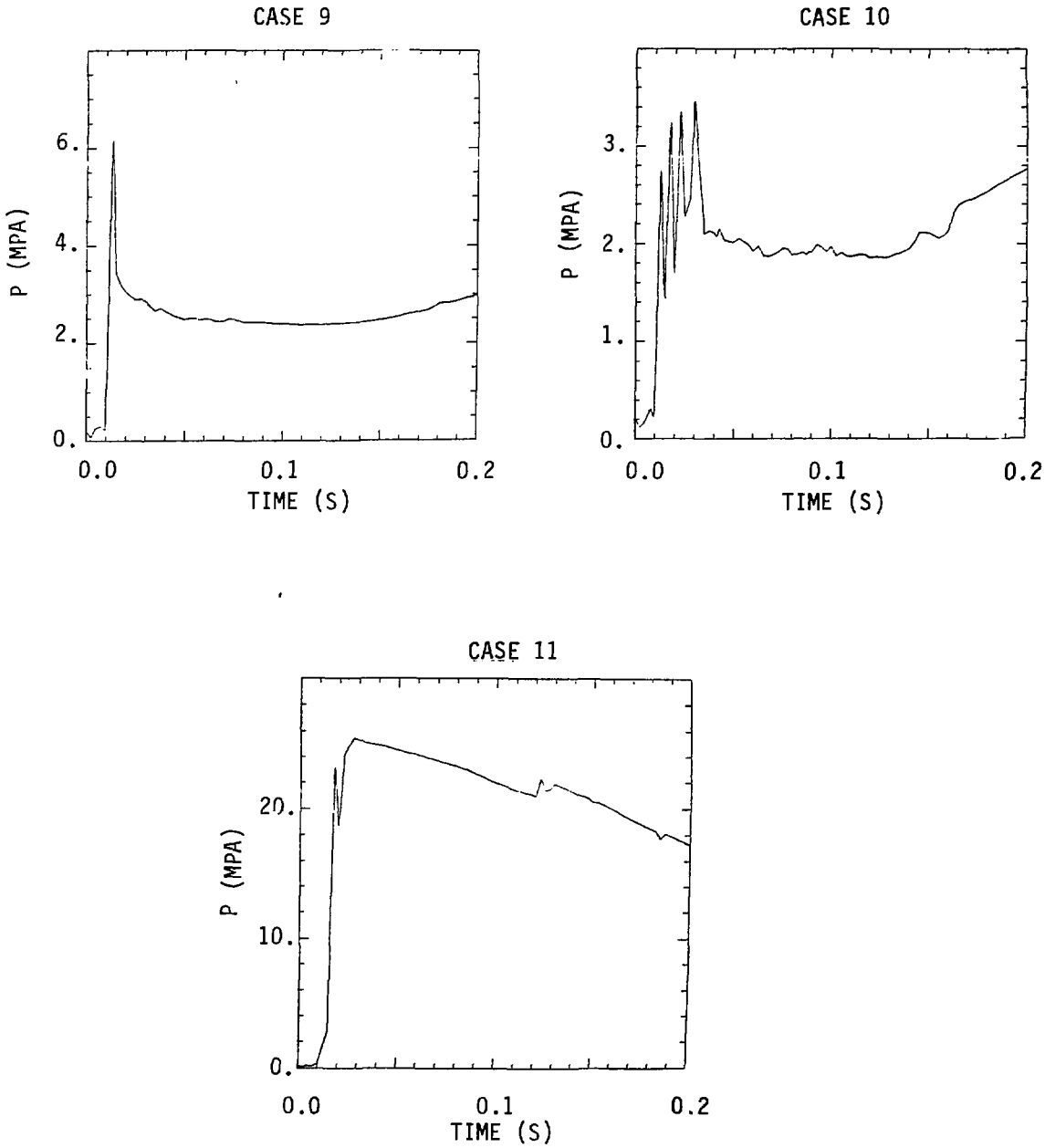

Fig. 13. (cont.)
Blanket-subassembly midplane pressure vs time for each case.

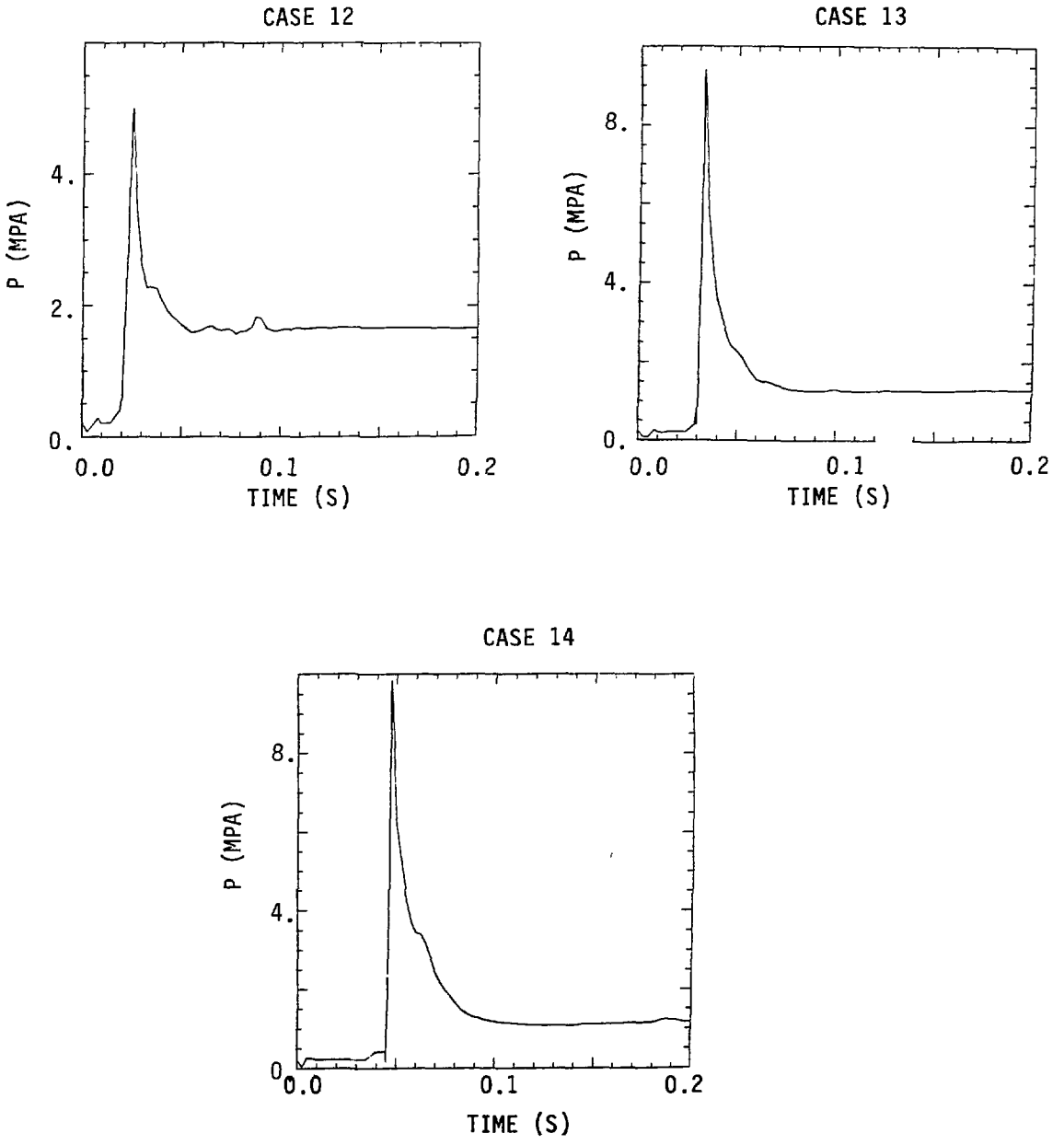

Fig. 13. (cont.)
Blanket-subassembly midplane pressure vs time for each case.

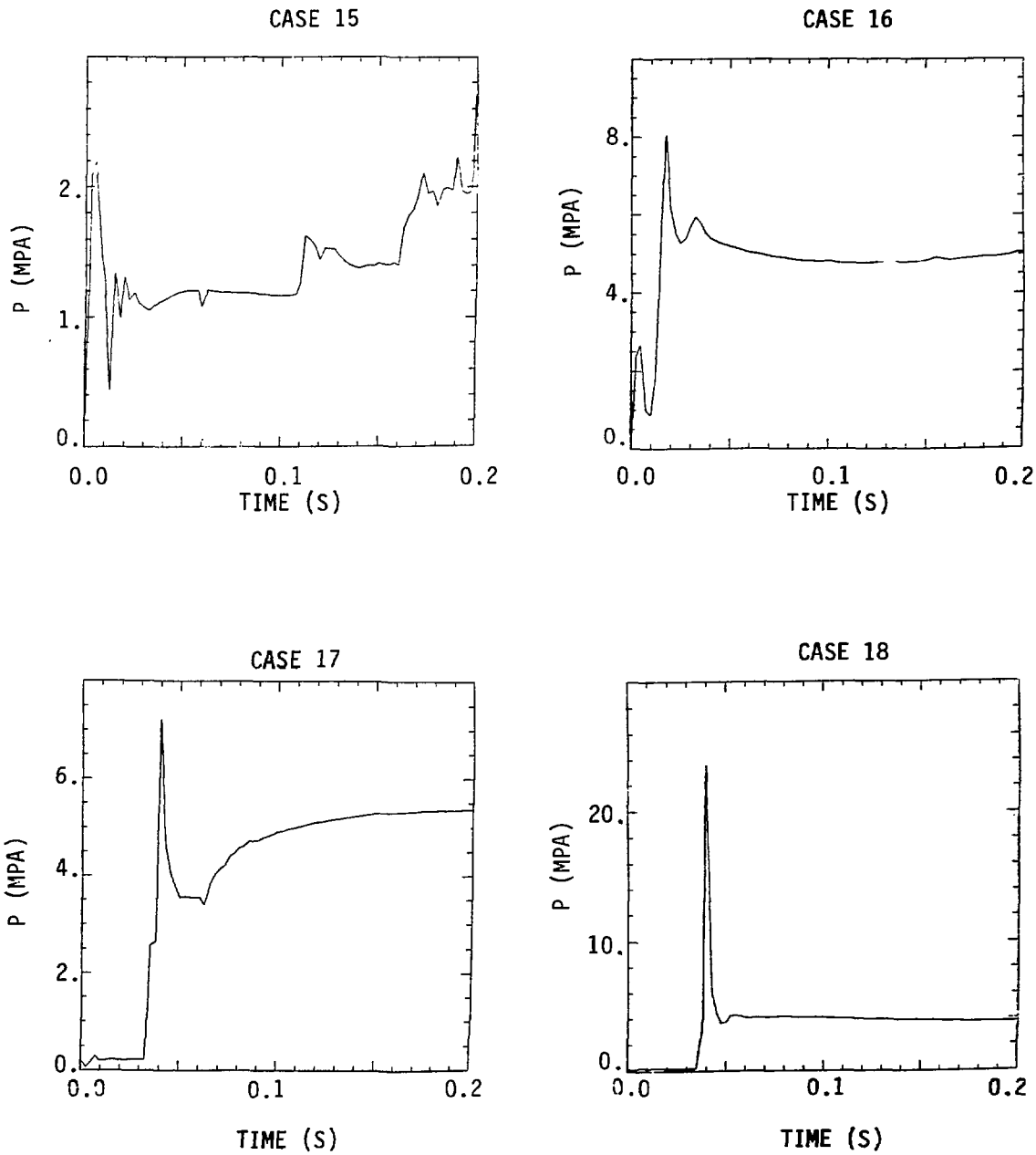

Fig. 13. (cont.)
Blanket-subassembly midplane pressure vs time for each case.

Cases 2 and 12, but with relaxed pressures very nearly the same in corresponding cases.

The work potential of the molten pool is changed monotonically by changing its pressure. This is perhaps the most important effect of the pool-sodium interaction. An examination of the pool pressure changes for the various cases shows a maximum change for Case 11 in which the entire subassembly wall failed very rapidly. This suggests that the greater the rate of subassembly wall failure (relative to the liquid sodium expulsion rate) the greater the work potential that will result.

2. Sodium Vapor Mass. The total sodium vapor mass in the system had a time history similar to the pressure (Fig. 14). There was an initial peak in the vapor mass of about 0.05 kg followed by a sharp decrease because of condensation. Subsequent behavior was typically governed by vapor production that occurred as a result of interactions with hot material, eventually expelling the liquid sodium from the subassembly. The initial sodium vapor mass varied because sodium vapor provided the initial pool pressure. Higher pressures and lower temperatures in the fuel-steel pool required more sodium vapor to achieve the desired initial conditions.

Increasing pool temperature, pool pressure, liquid-liquid heat transfer, or subassembly flow or decreasing the subassembly wall break area caused the sodium vapor mass at later times to be greater than the initial peak value. Cases 9 and 10 show that decreasing the breach area decreased the total sodium vapor mass produced. Only in Case 11, where the subassembly wall was allowed to fail throughout the entire active core region, was significant vapor mass produced. Cases 12, 13, and 14 show that the location of the breach in the active core region had only a minor effect on the net sodium vapor mass.

3. Sodium Liquid Mass in the Active Core. It was expected that the timing and rate of liquid sodium expulsion from the active core region might be a sensitive function of some variations in input parameters that were considered. In most cases no great sensitivity was apparent (Fig. 15). Exceptions were Cases 13 and 14 where the breach was located at the top or the bottom of the active core; in these cases there was a considerable delay in sodium expulsion. In Case 15 sodium was never driven out the bottom of the subassembly because the sodium inlet pressure was almost an order of magnitude greater than the initial pool pressure.

Finally in Case 11 the entire active core region subassembly wall (nodes J = 9 to 17) failed simultaneously. The resulting pool-sodium interaction

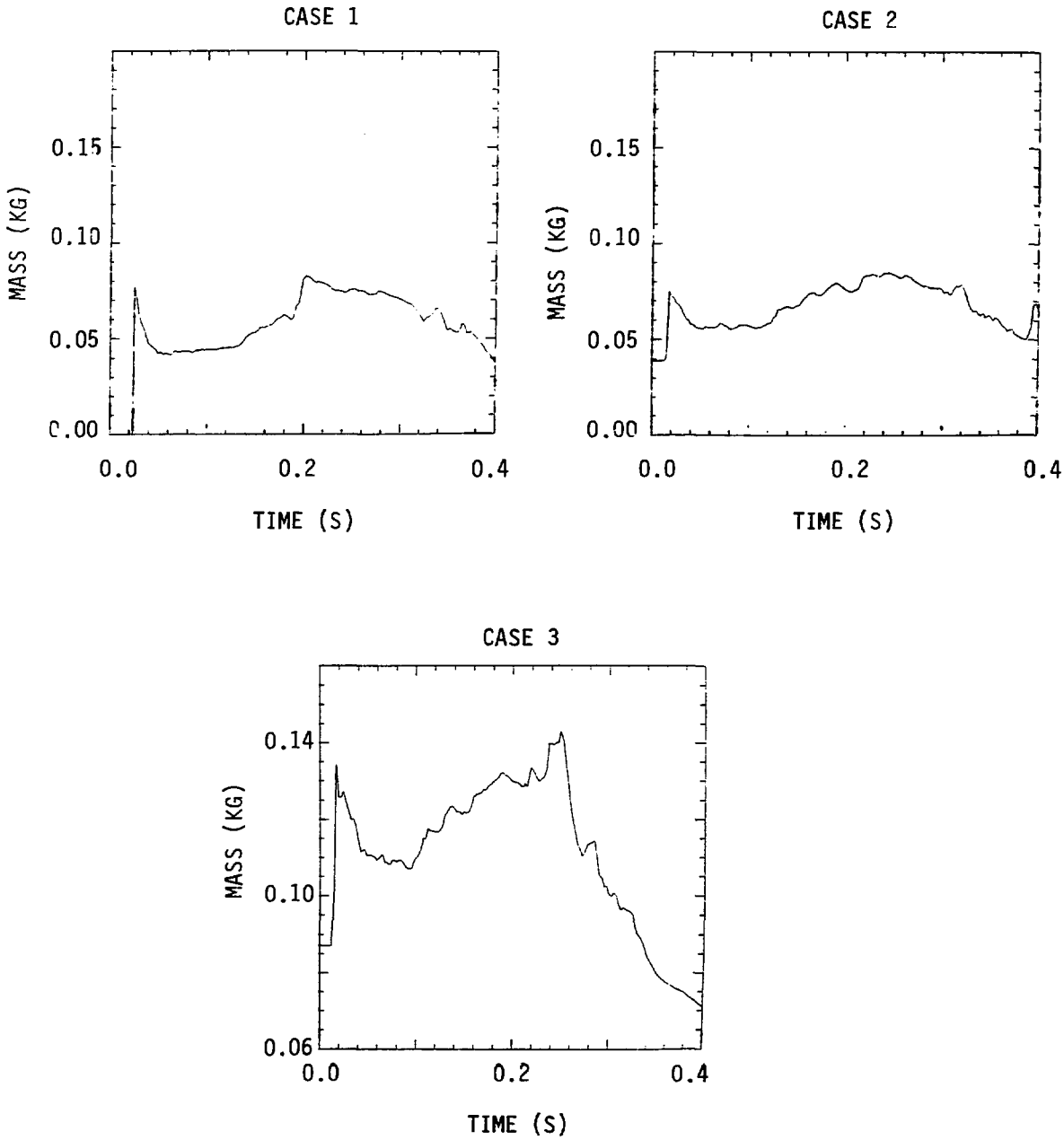

Fig. 14.
Total system sodium vapor mass vs time for each case.

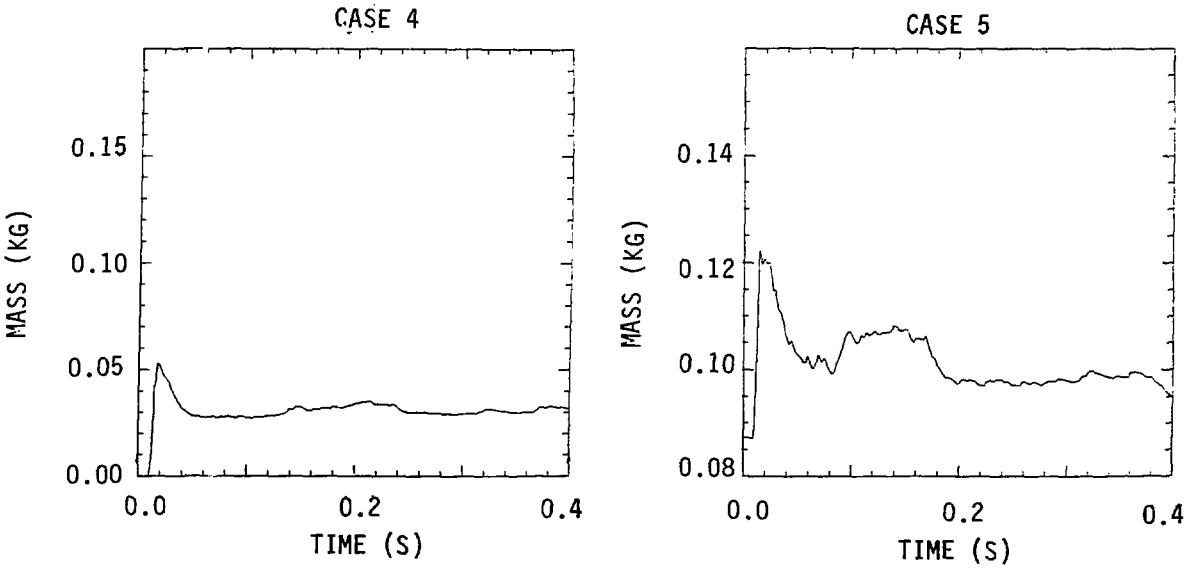

Fig. 14. (cont.)
Total system sodium vapor mass vs time for each case.

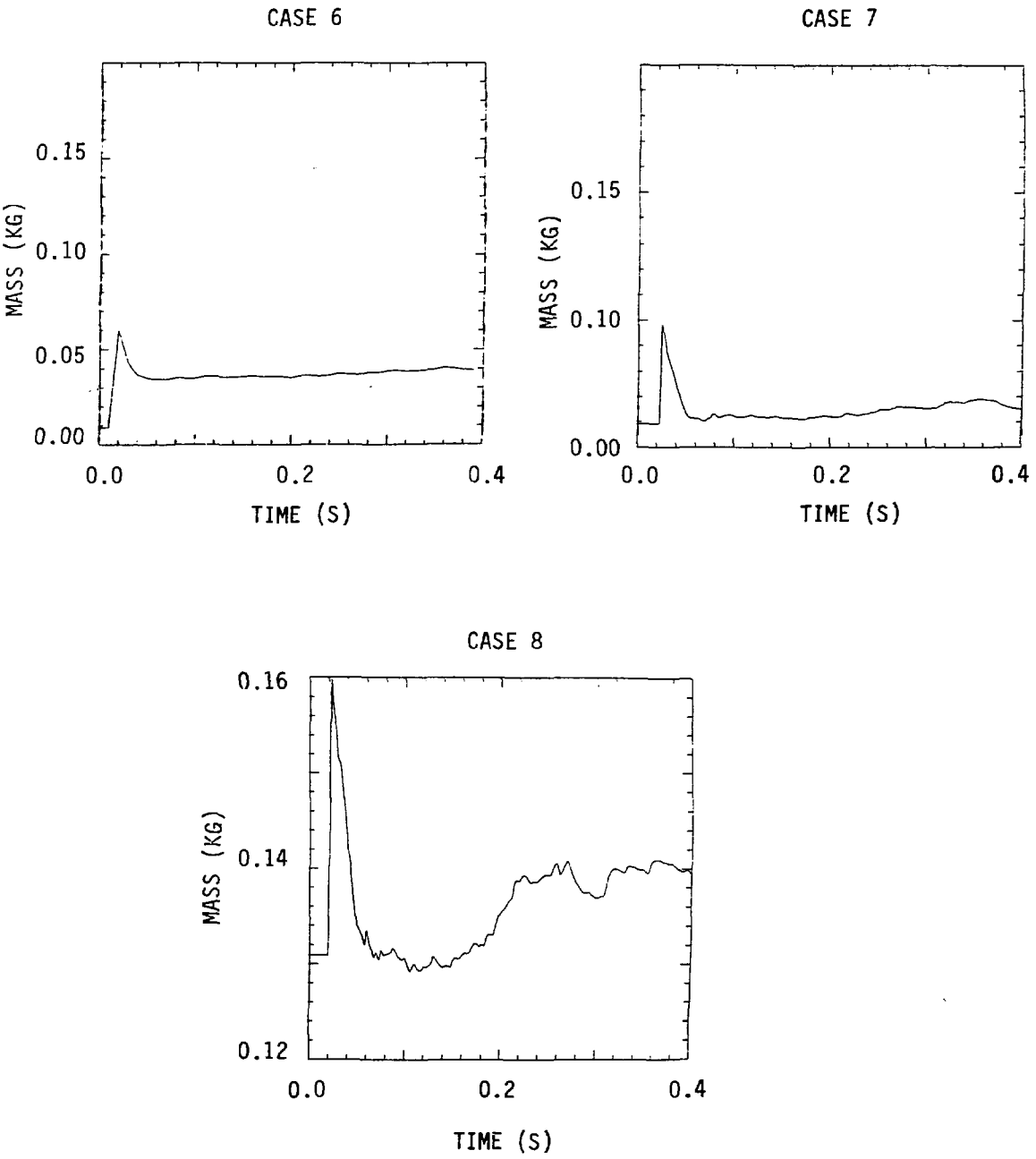

Fig. 14. (cont.)
Total system sodium vapor mass vs time for each case.

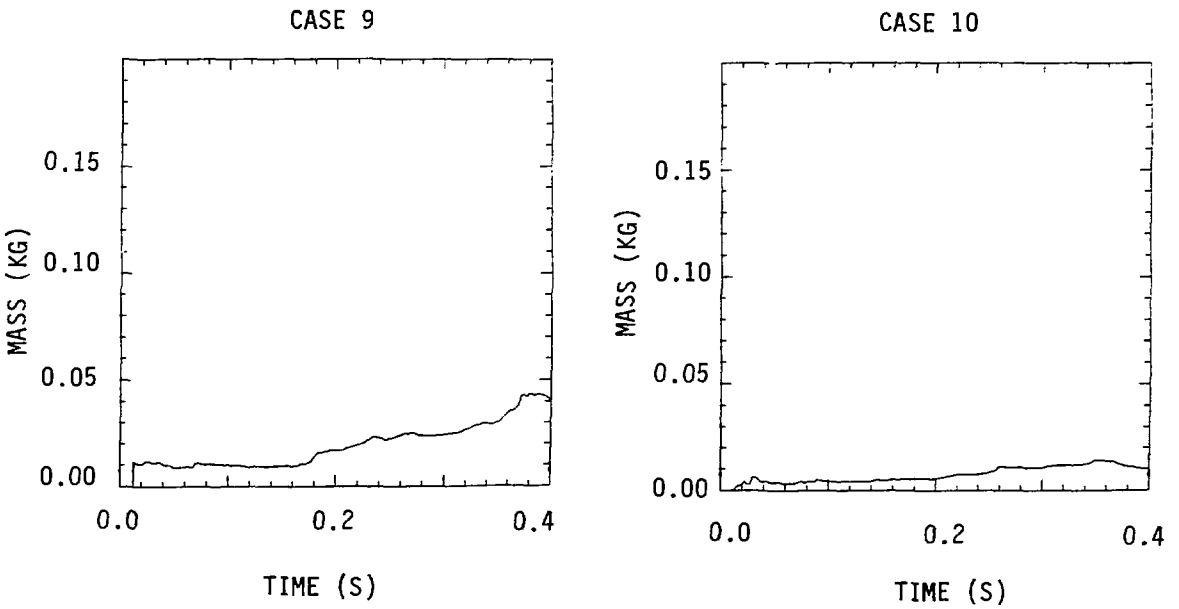

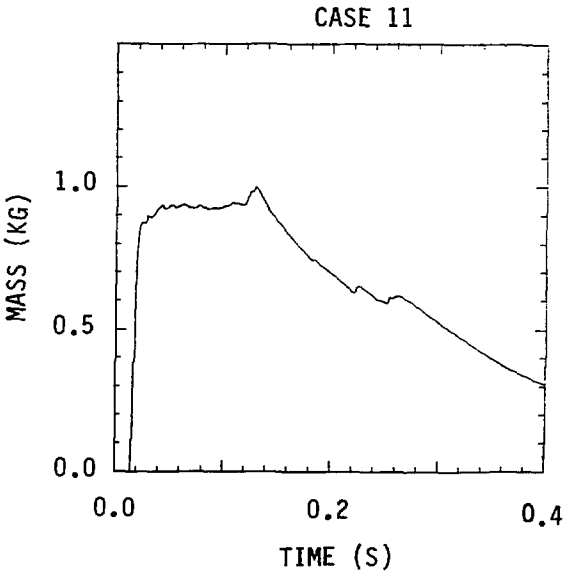

Fig. 14. (cont.)
Total system sodium vapor mass vs time for each case.

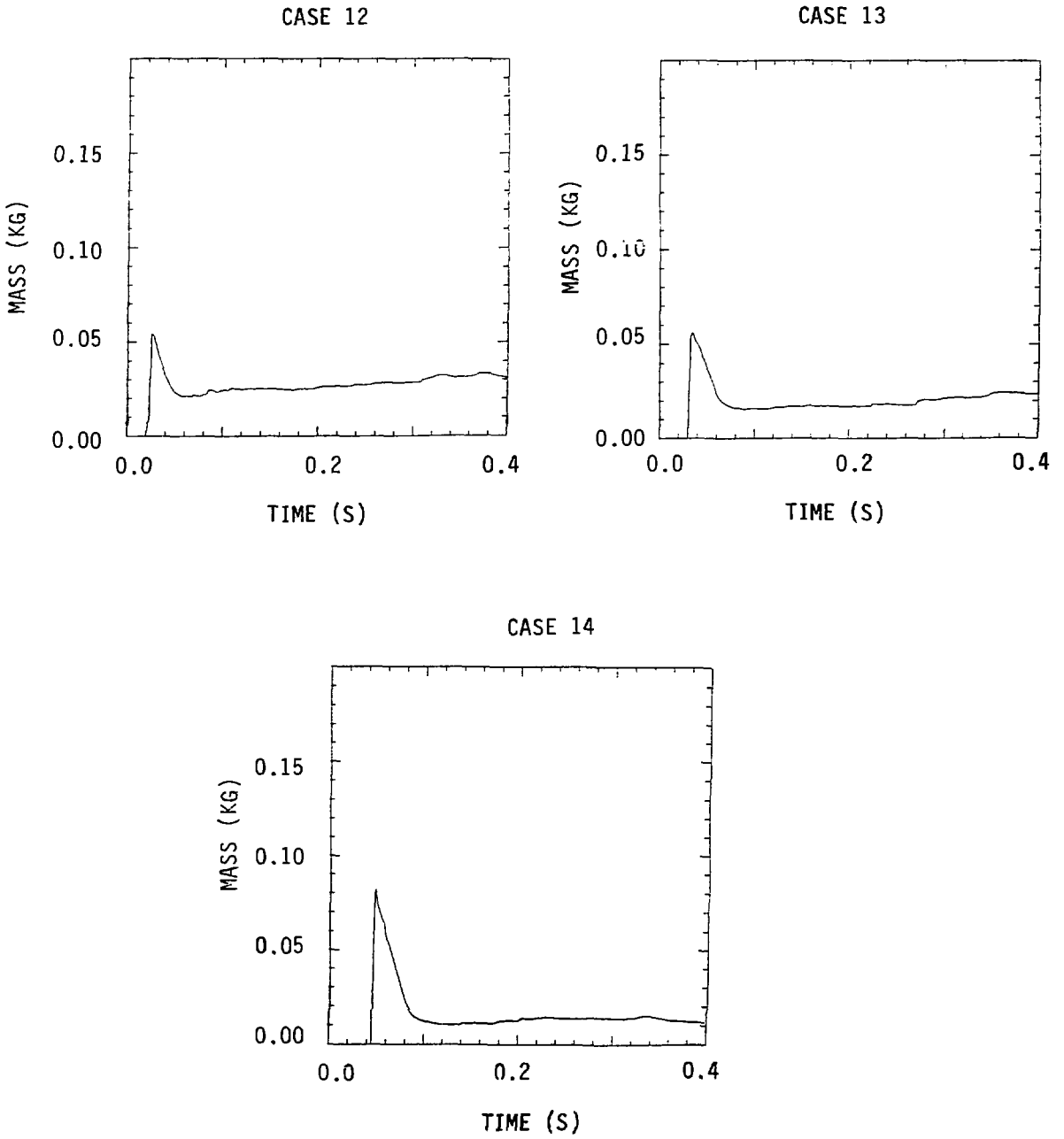

Fig. 14. (cont.)
Total system sodium vapor mass vs time for each case.

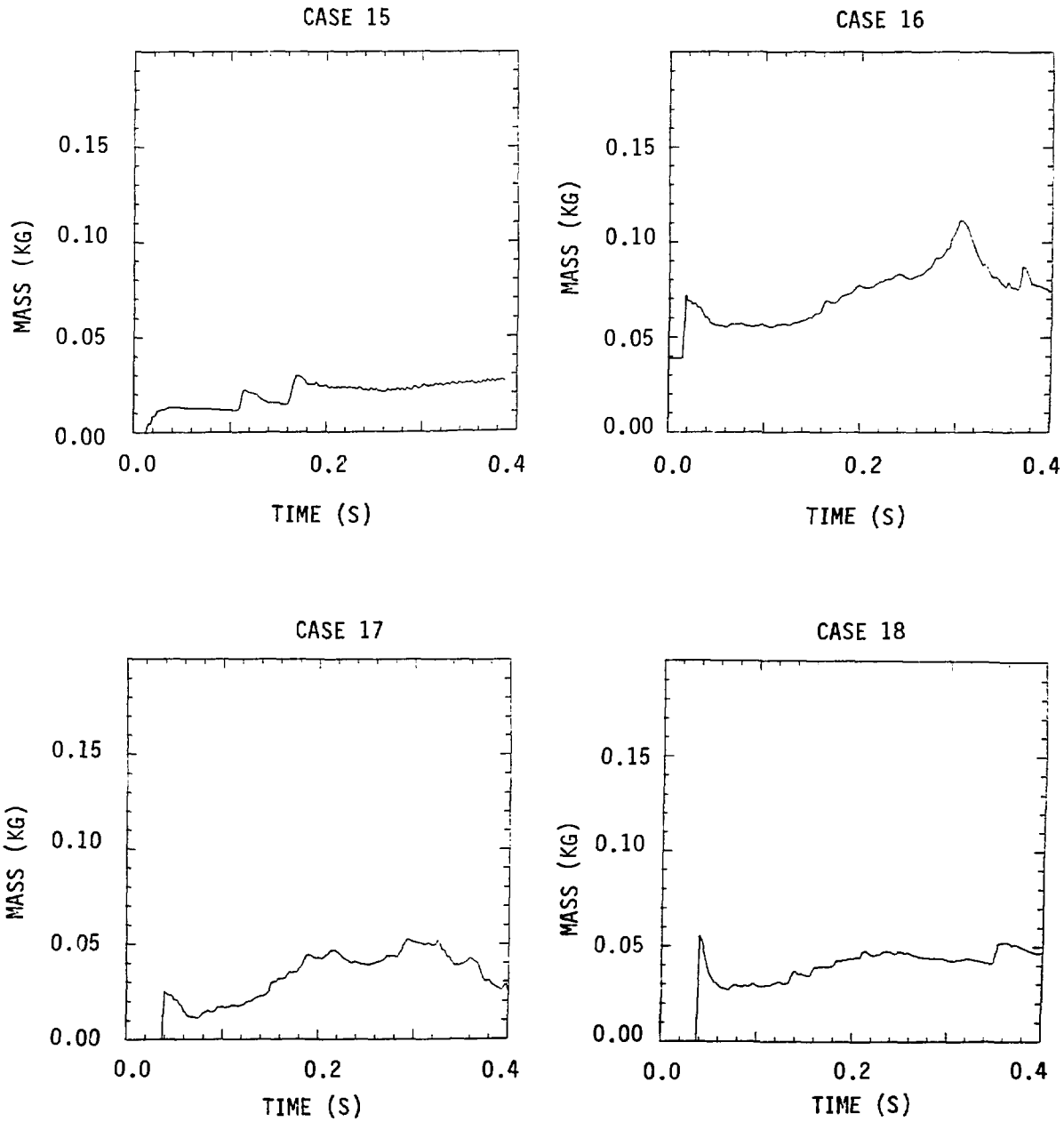

Fig. 14. (cont.)
Total system sodium vapor mass vs time for each case.

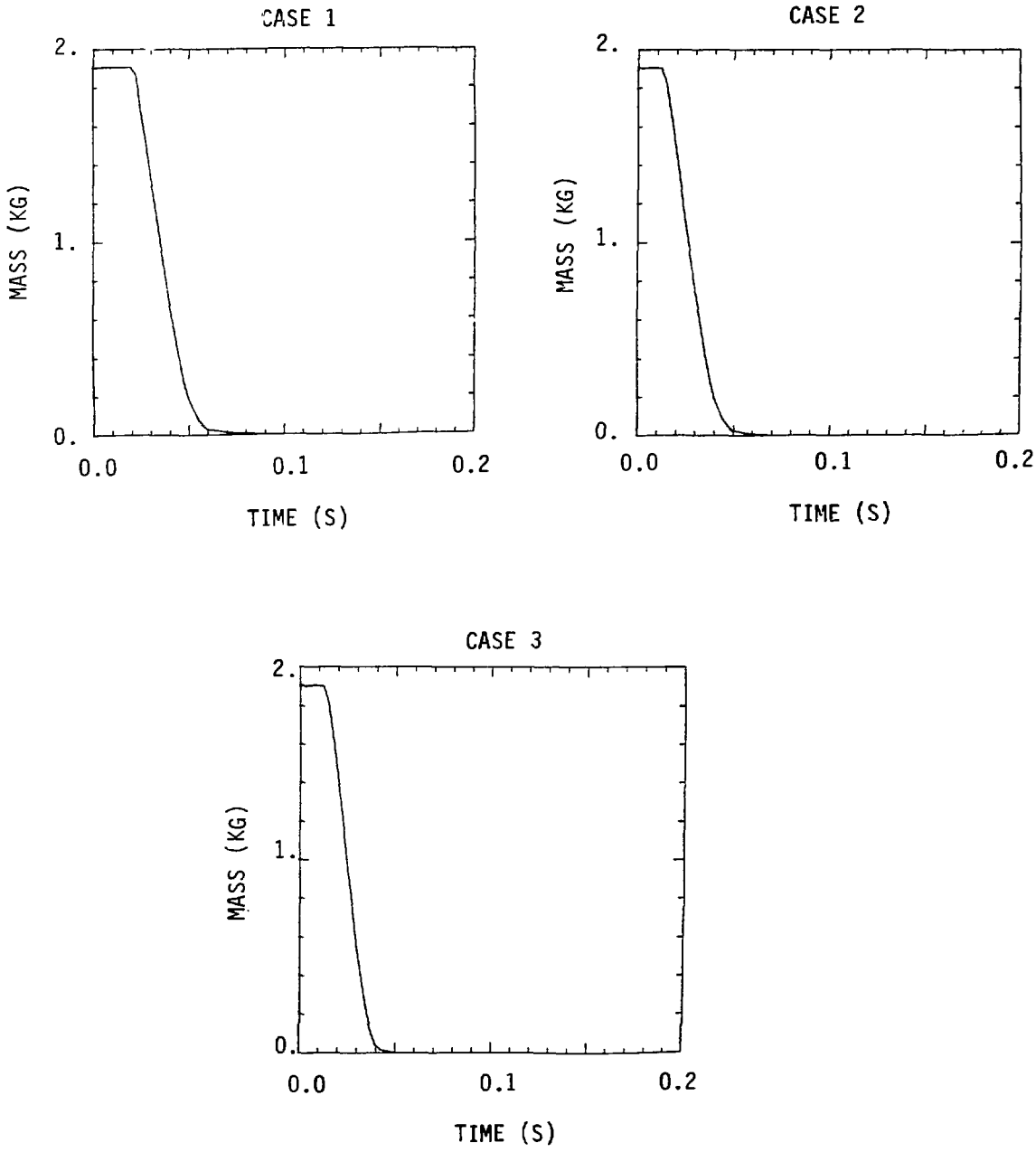

Fig. 15.
Sodium liquid mass in the active core region vs time for each case.

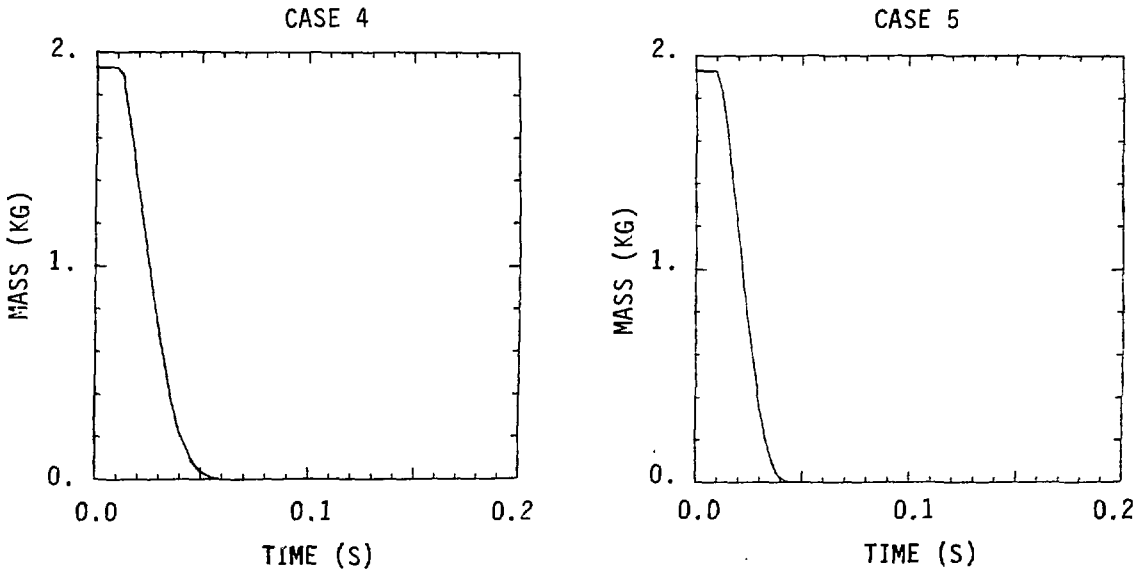

Fig. 15. (cont.)
Sodium liquid mass in the active core region vs time for each case.

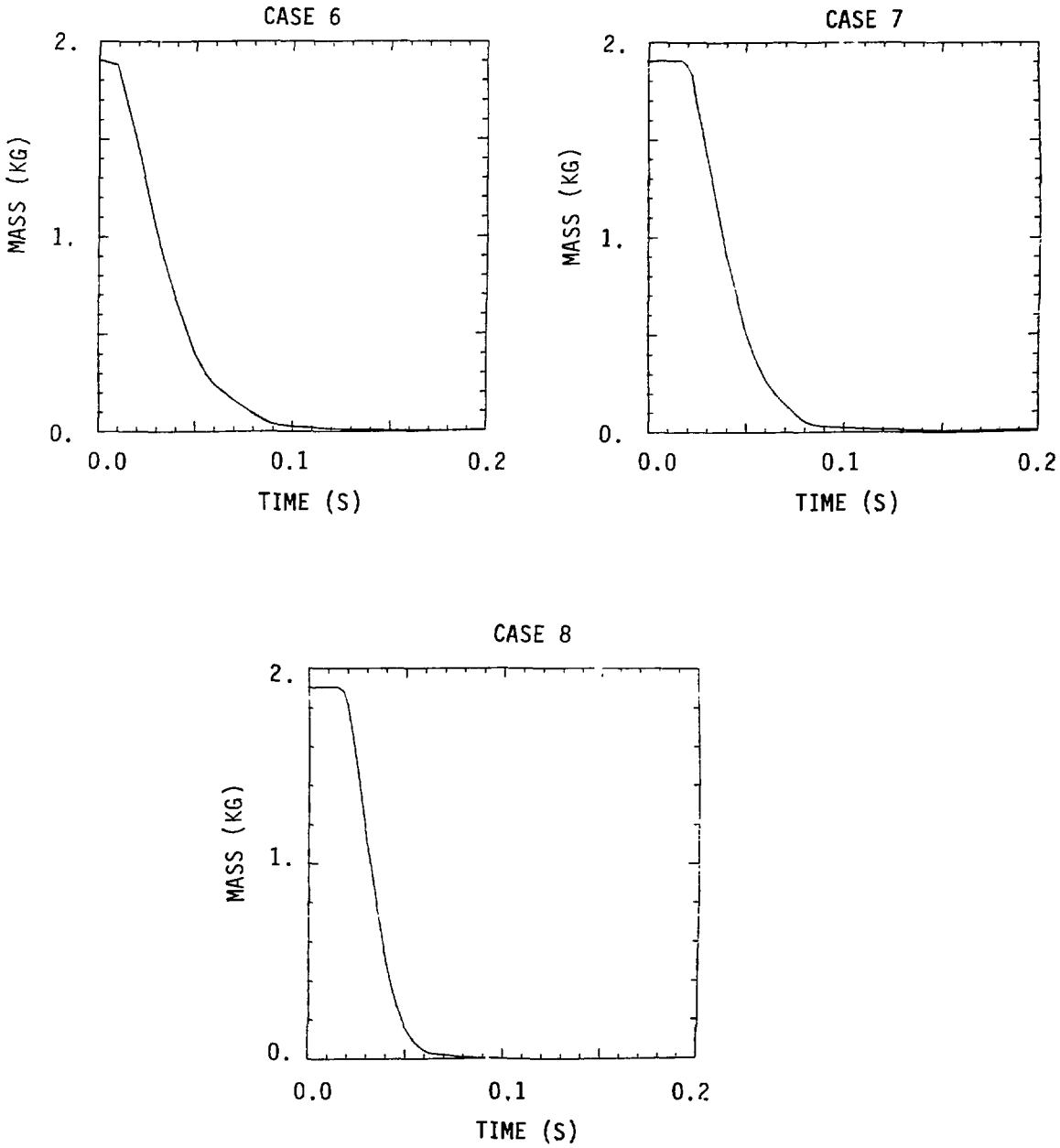

Fig. 15. (cont.)
Sodium liquid mass in the active core region vs time for each case.

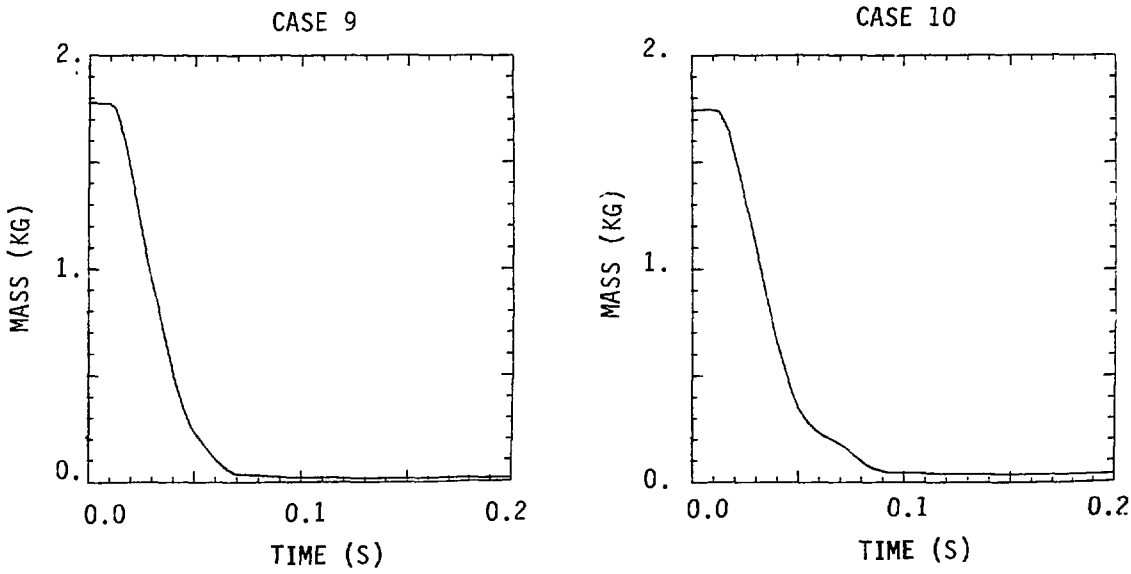

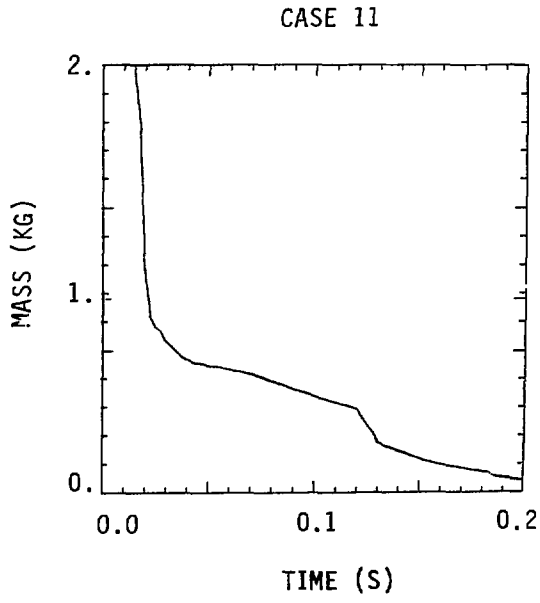

Fig. 15. (cont.)
Sodium liquid mass in the active core region vs time for each case.

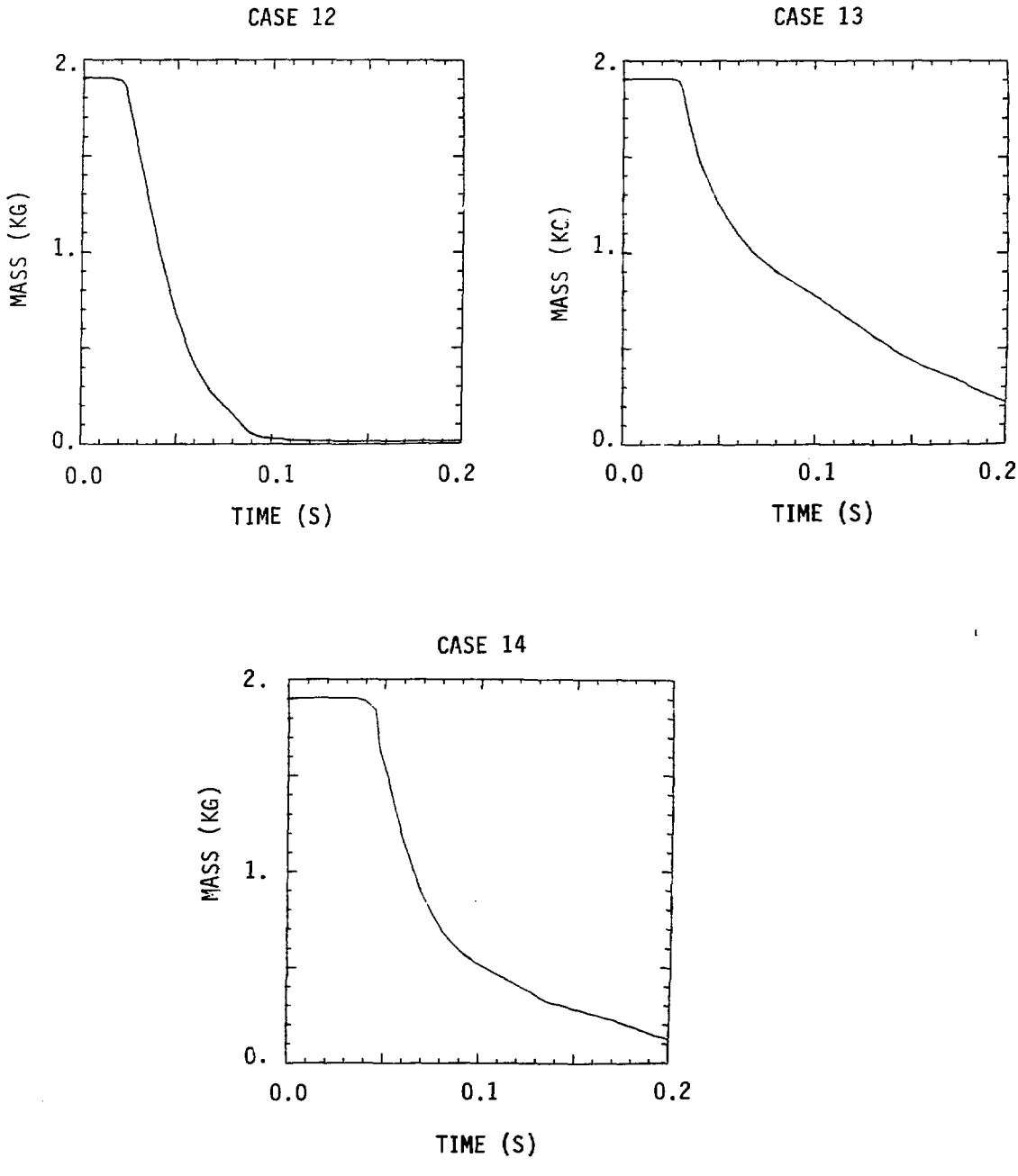

Fig. 15. (cont.)
Sodium liquid mass in the active core region vs time for each case.

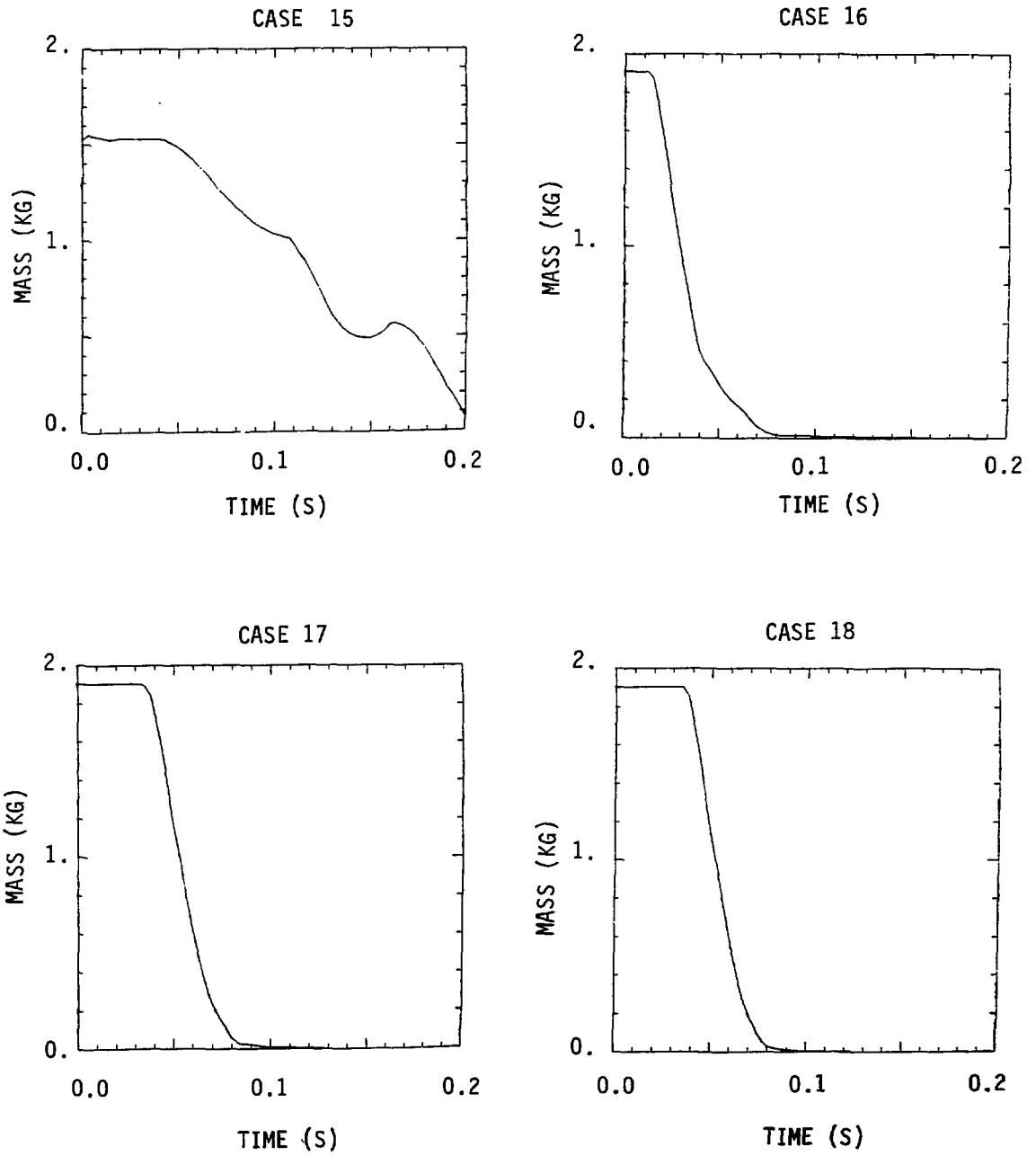

Fig. 15. (cont.)
Sodium liquid mass in the active core region vs time for each case.

pressurized, quite uniformly, the pool and the active core. However, in this case pool material was not constrained radially near its axial boundaries and moved quickly into the subassembly. Enhanced mixing of pool and sodium materials led to rapid sodium vaporization causing coolant to be expelled from both ends of the active core region. The coolant in the seven nodes at the center of the core, however, was contained by opposing strong axial pressure gradients and, except for Ring 3, was trapped in this region for a time long compared to sodium expulsion times of the other cases.

4. Cladding Mass in the Core. Figure 16 records the time history of the cladding in the region of the active core plus the axial blankets (nodes J = 5 to 21). These curves show a rapid melting of most of the cladding in the core followed by much slower melting of the remaining cladding. The latter was a two-dimensional effect which reflected the delayed removal of sodium in the outer radial node in the active core. This effect was not present in the one-dimensional model of the subassembly (Cases 4 and 5) where complete cladding meltout was observed.

There was a direct correlation between initial pool pressure and the times of cladding failure in Cases 1, 2, and 3. Greater initial pool pressure led to earlier cladding relocation because of earlier sodium expulsion. Also Cases 6, 7, and 8 show that a lower initial pool temperature considerably delayed cladding melting. Cases 9 and 10 indicate that decreasing the subassembly breach area delayed cladding failure, whereas Case 11 shows that both liquid sodium and cladding remained trapped in the center of the core for an extended period.

A comparison of Cases 13 and 14 with Case 12 indicates that moving the location of the breach away from the axial midpoint of the active core delayed the cladding failure process.

Comparing Case 16 with Case 2 shows that increasing the pressure at the bottom of the subassembly merely delayed the final cladding failure slightly.

Case 15, with low pool pressure and high sodium inlet pressure, shows very slow cladding meltout because of the slow introduction of the hot fuel-steel pool mixture.

Finally, when Cases 17 and 18 are compared to Case 1, one sees that major changes in the liquid-liquid heat-transfer multipliers had no discernible effect on the time history of cladding failure.

5. Pressure Difference Across the Subassembly Wall. The difference between the internal and the external fluid pressures on the subassembly wall

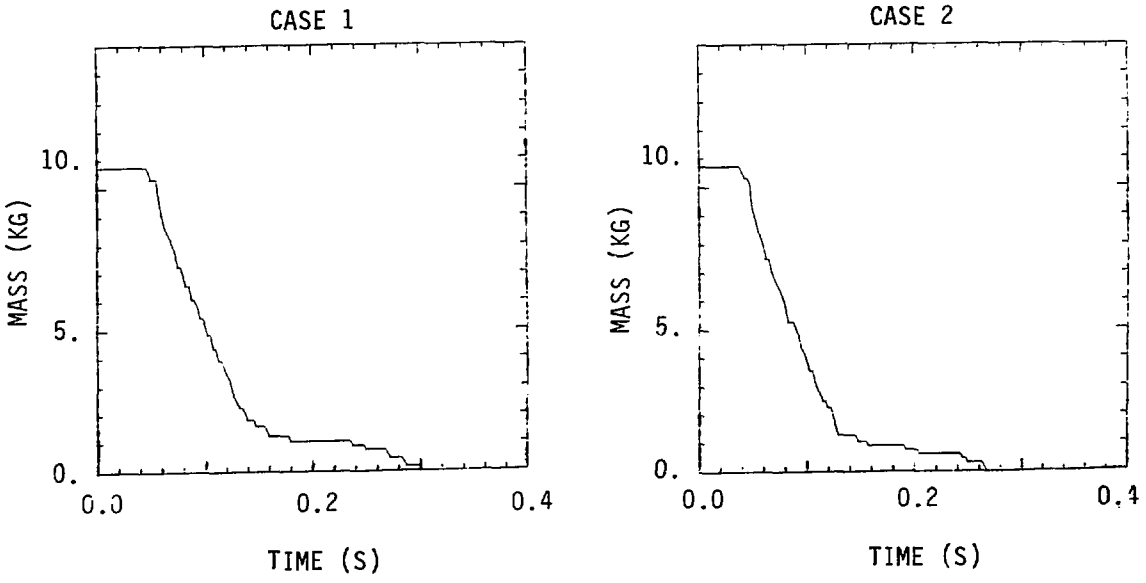

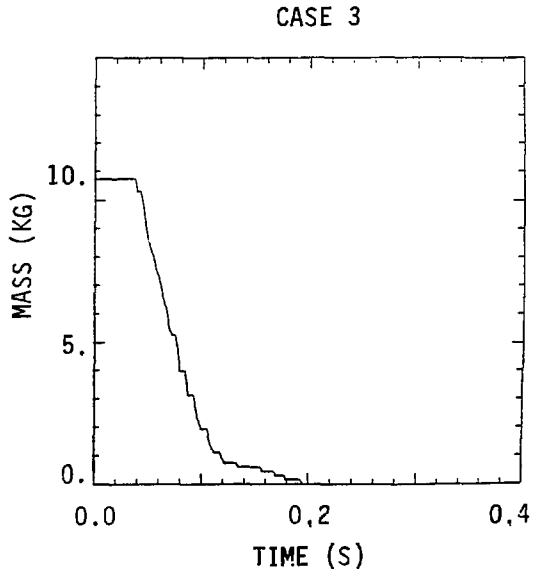

Fig. 16.
Cladding mass in the core plus axial blankets vs time for each case.

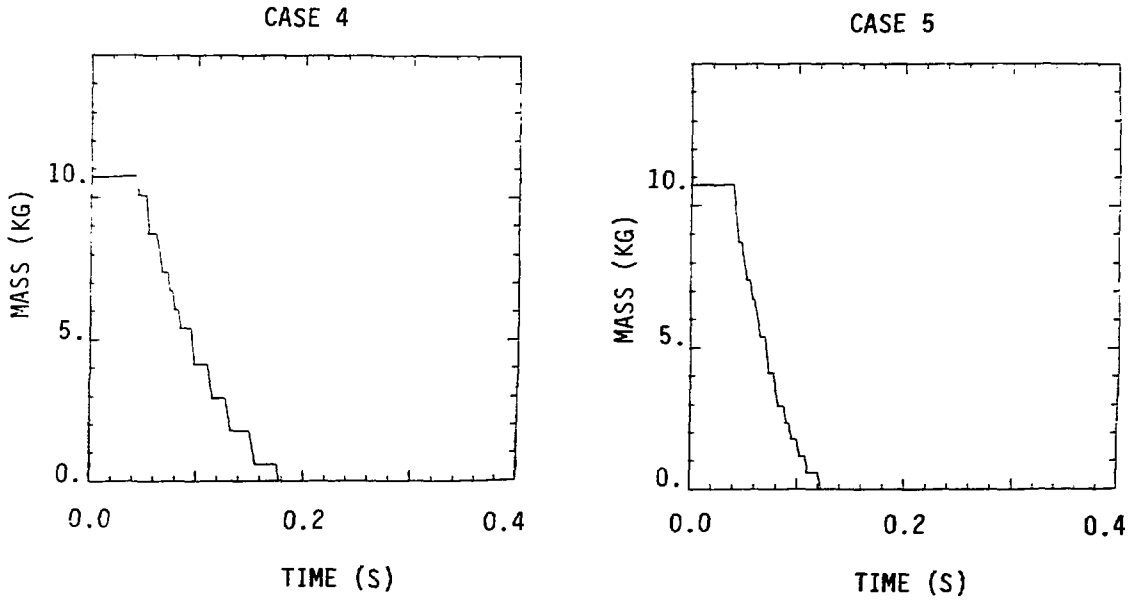

Fig. 16. (cont.)
Cladding mass in the core plus axial blankets vs time for each case.

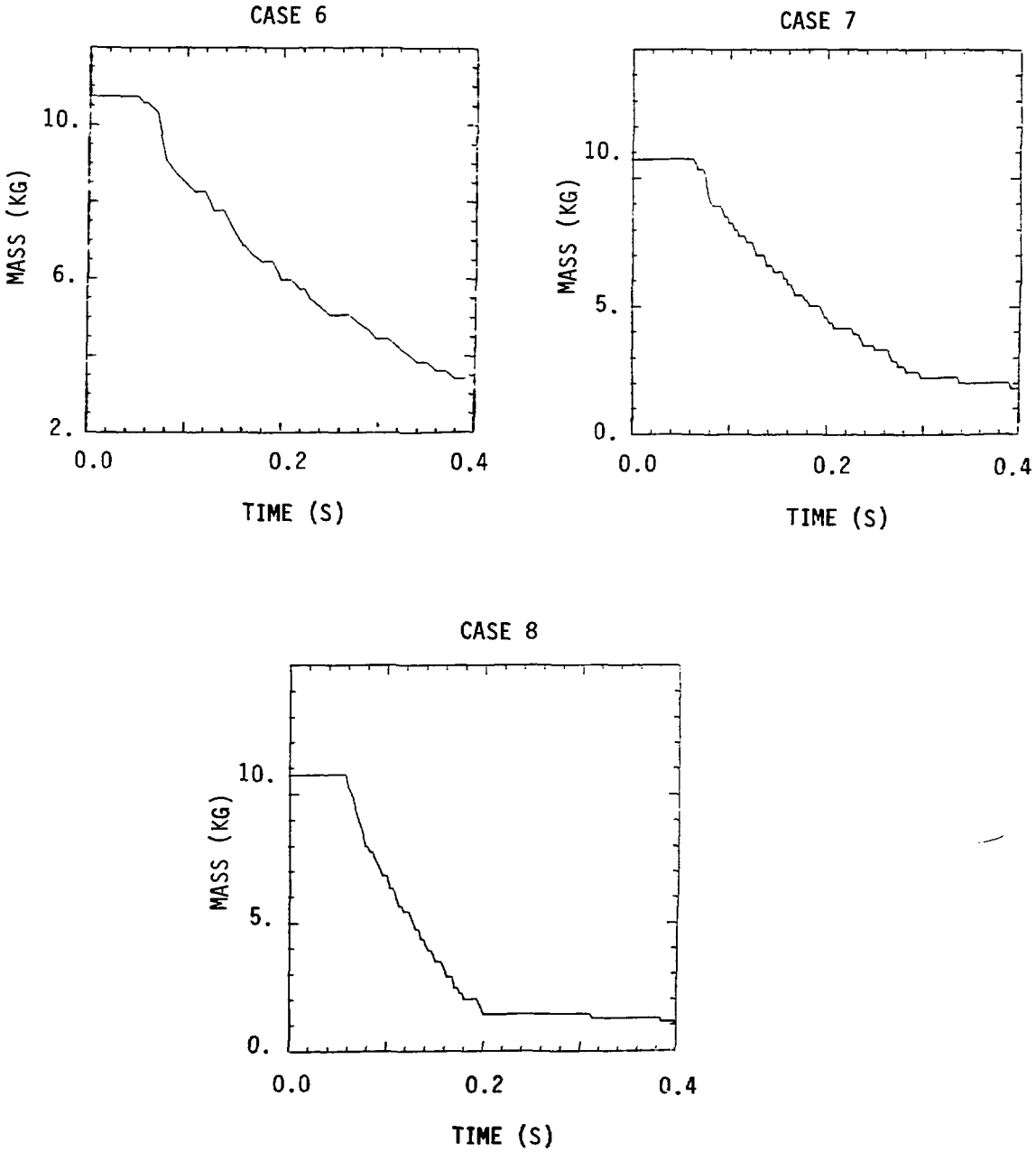

Fig. 16. (cont.)
Cladding mass in the core plus axial blankets vs time for each case.

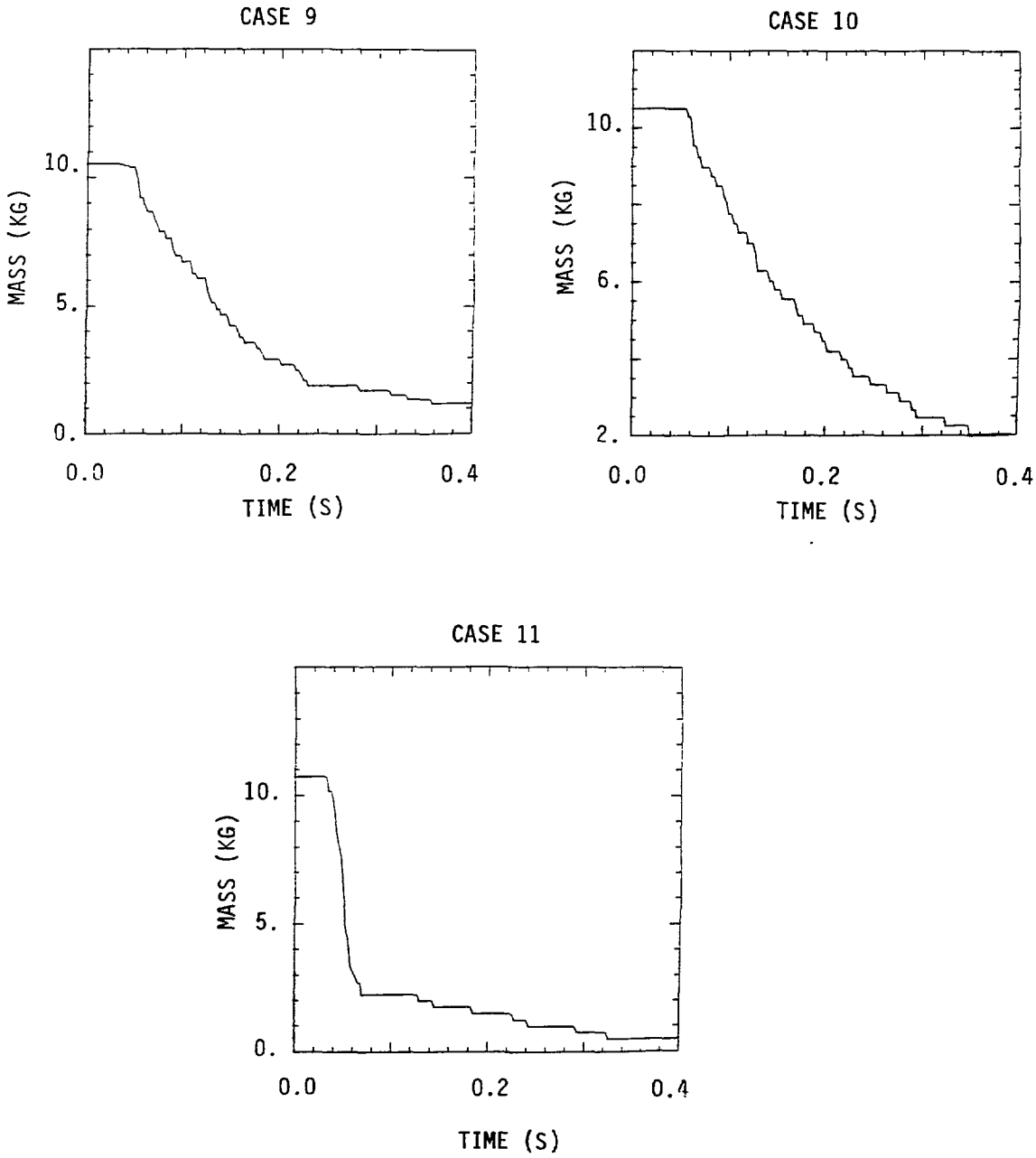

Fig. 16. (cont.)
Cladding mass in the core plus axial blankets vs time for each case.

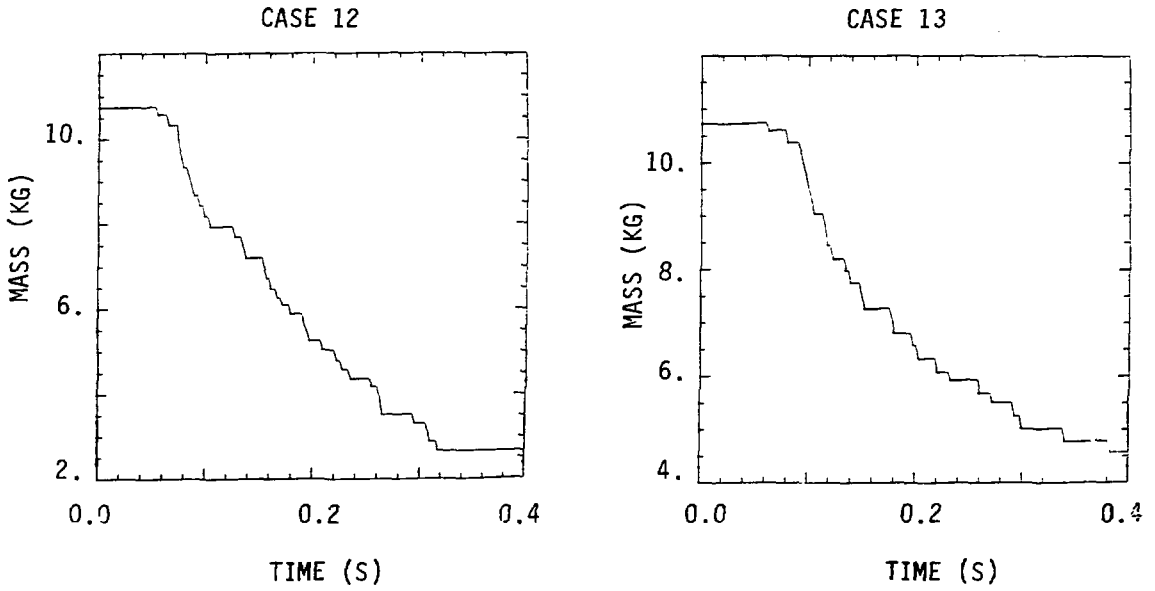

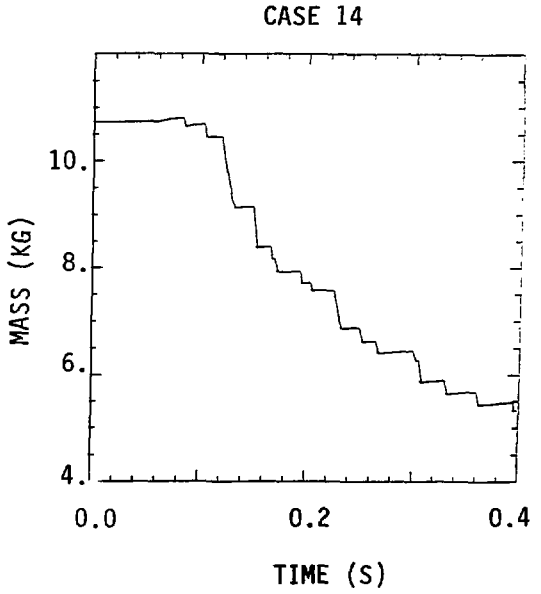

Fig. 16. (cont.)
Cladding mass in the core plus axial blankets vs time for each case.

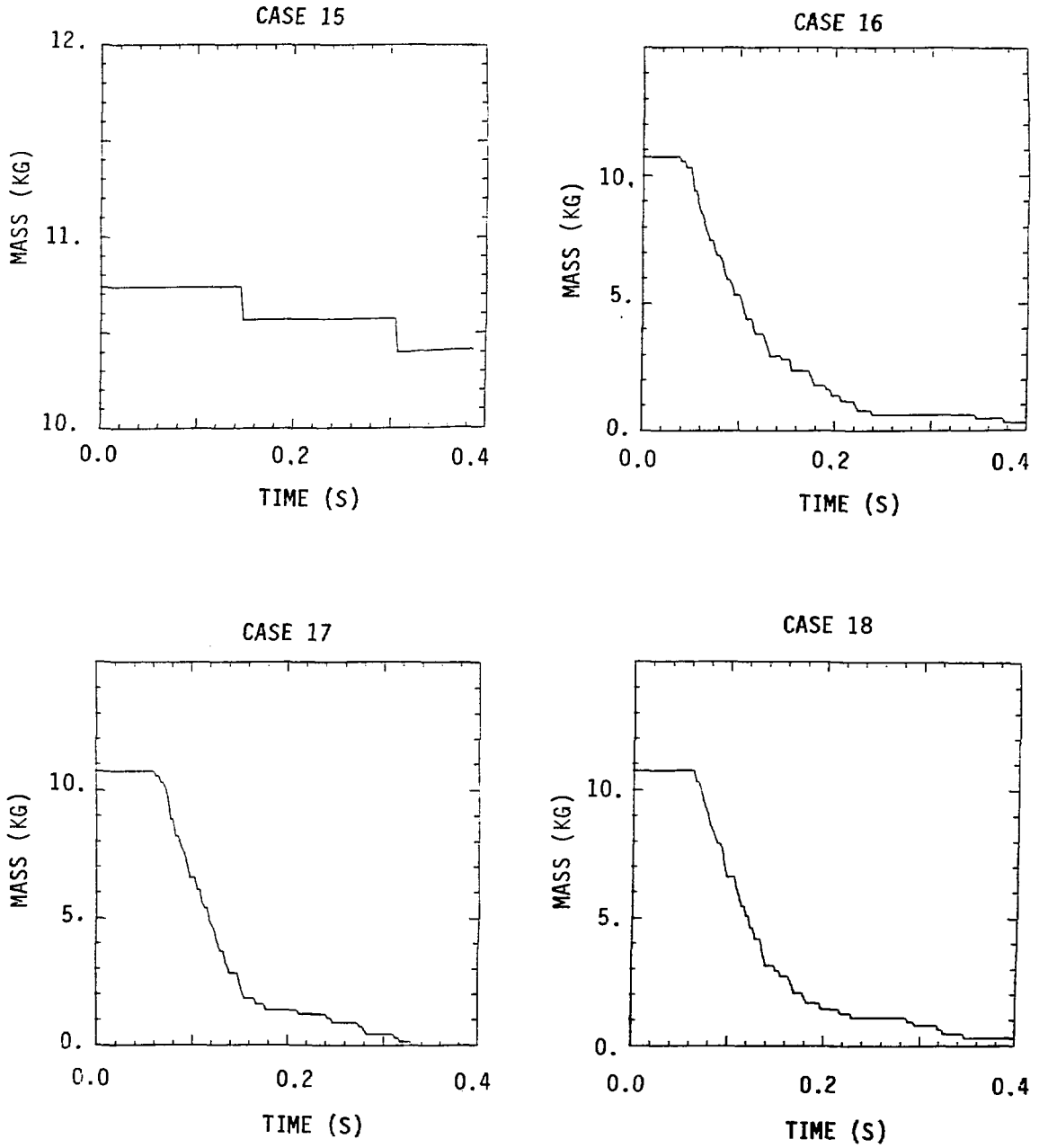

Fig. 16. (cont.)
Cladding mass in the core plus axial blankets vs time for each case.

at a node (J = 14) immediately above the crack opening is given in Fig. 17 for Cases 1, 2, and 3. These are the results of high pool temperature (4800 K) calculations with varying initial pool pressures. Of these, Cases 2 and 3 gave the greater and almost equal values of 2.6 MPa.

Appendix B outlines a calculation of the hoop stress generated in a can wall because of applied pressures and an imposed radial temperature distribution. This calculation shows that to mechanically develop a tensile hoop stress, the inner pressure on the can wall must be greater than the outer pressure. This only occurred during our transient SIMMER-II calculations for periods of about 2 ms. In general tensile thermal hoop stresses will be induced by a temperature difference across the can walls.

For Case 3 and the pressure difference above, Eq. (B-7) gives a value for the hoop stress of 48.2 MPa as compared with the ultimate tensile strength for walls at 1225 K of 10^2 MPa. However, it would only take a temperature difference of 200-300 K to give a thermal contribution of this order to the stress. Because we have considered only cases with a prescribed initial crack, the induced hoop stress may indeed have been sufficient for crack propagation.

V. SUMMARY, OMISSIONS, AND FUTURE OBJECTIVES

We have made a parametric study with SIMMER-II of the interaction of a blanket subassembly with a molten fuel/steel pool via subassembly wall failure. Among the parameters that were varied were the subassembly wall opening geometry, the pool injection pressure and temperature, the blanket coolant flow, the liquid-liquid heat transfer, and the number of radial calculational cells.

A typical calculation showed initial coolant interaction with molten fuel/steel after subassembly wall failure creating pressures of the order of tens of atmospheres. This was followed by pool material moving to the axial extremities of the pool. The rebounding pool material then interacted with subassembly sodium again on a longer time scale and eventually expelled the liquid sodium from the subassembly. By this time the pool pressure, in most cases, had relaxed to a stable value. There was sufficient entrainment of noncondensable sodium vapor into the pool to maintain this pressure. The final value was in many cases greater than the initial pool pressure; this was

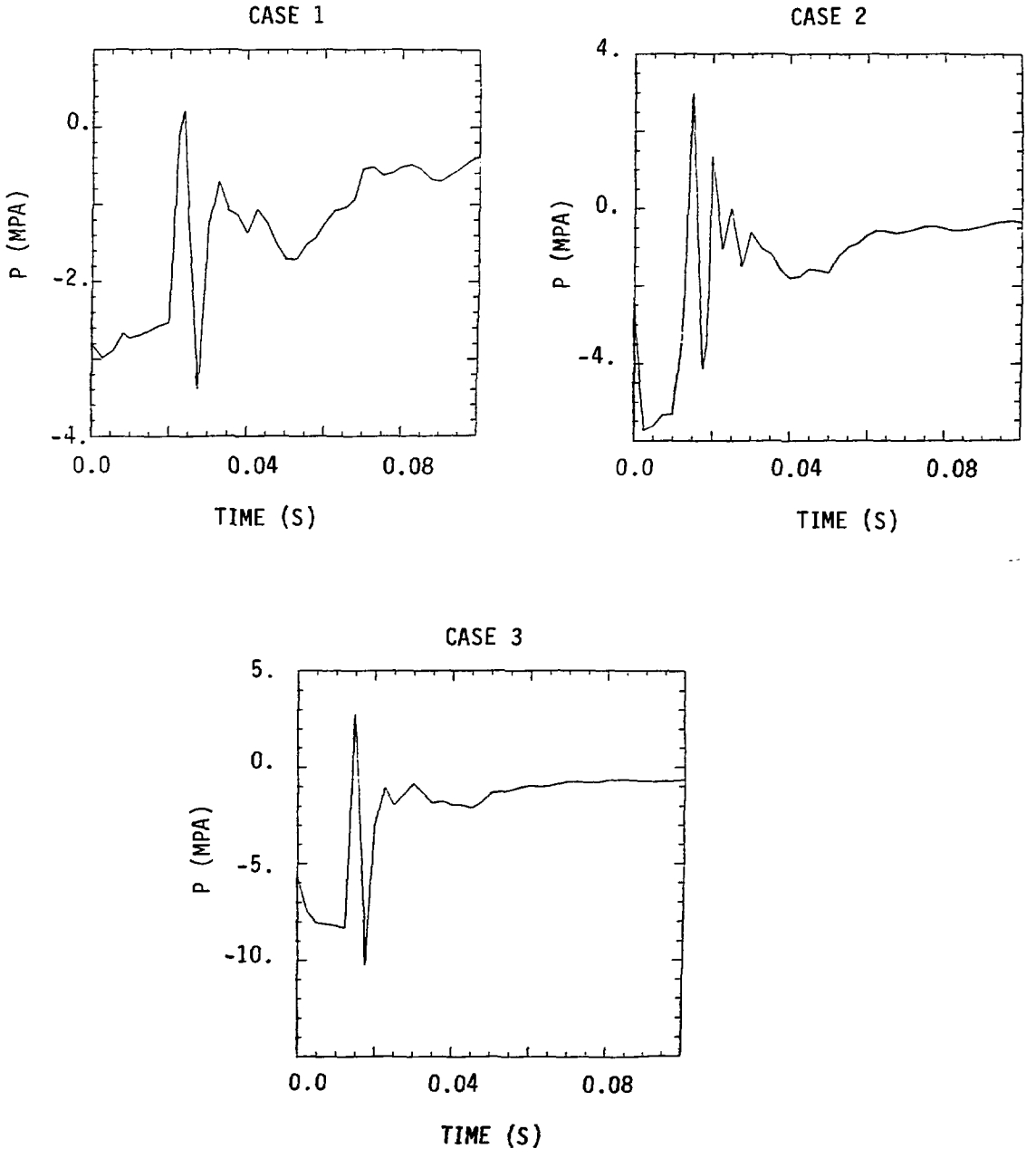

Fig. 17.
Pressure difference across the subassembly wall at core midplane vs time for selected cases.

particularly true for those cases that involved either the larger subassembly wall openings or the lower initial pool pressures.

In general we conclude that the resulting pressurization of the pool is a good figure of merit for rating the severity of the event. This pressurization depends strongly on the mixing of the fuel/steel with the sodium. In turn, the mixing is a strong function of the

a. initial subassembly wall opening size,

b. initial pool pressure,

c. wall failure rate relative to sodium removal rate.

Future studies will

a. allow variations in the mode of wall failure by incorporation of better models for crack failure and propagation,

b. consider the effects of multiple wall failures in space and time, and

c. consider a control subassembly as a possible avenue for core fuel removal.

Finally, the version of SIMMER-II used in this study did not contain a pellet breakup model; future calculations will incorporate such a model because pool material melted most of the cladding and this could have a considerable effect on subsequent behavior.

REFERENCES

1. Letter, C. R. Bell (Los Alamos) to D. R. Ferguson (TMC), Task 1 of the Los Alamos program entitled LOA-3, Energetics Accommodation, Q-7-81-R92, April 8, 1981.

2. L. L. Smith, "SIMMER-II: A Computer Program for LMFBR Disrupted Core Analysis," Los Alamos Scientific Laboratory report NUREG/CR-0453, LA-7515-M (October 1978).

3. J. F. Jackson and M. G. Stevenson, Compilers, "Nuclear Reactor Safety Quarterly Progress Report April 1 - June 30, 1979," Los Alamos Scientific Laboratory report NUREG/CR-0993, LA-7968-PR (August 1979).

APPENDIX A

ESTIMATION OF MAXIMUM FRACTURE AREA

We wish to estimate the maximum flow area that can be developed in a singly fractured subassembly duct. Assume the fracture occurs at a hexagonal subassembly corner (Fig. A-1) with a length equal to the height, h = 0.9144 m, of the active core. Further assume that the failed subassembly walls bow in circular arcs until they meet neighboring undeformed subassemblies.

The boundary of the fracture region can be considered to be the two circular arcs formed by two equal-radii circular rings that intersect at two points. This boundary and the line joining the two points determine the region indicated in Fig. A-2. For this case, where the core height h is much greater than the gap width, the flow area A into the subassembly is very nearly equal to twice the area determined by either circular arc and the common chord of intersection projected onto its plane of symmetry, or

$$A = 2 \cdot \frac{1}{2} r^2(\theta_0 - \sin\theta_0)\sin\frac{\pi}{6} \quad , \tag{A-1}$$

where r = 22.24 m is the radius of the circular ring and θ_0 = 0.04112 rad is the angle subtended on the circular ring by the intersection (see Fig. A-3). Thus we have

$$A = 2.866 \times 10^{-3}\ m^2 \quad , \tag{A-2}$$

which is equivalent to a square hole 2.107 inches on a side.

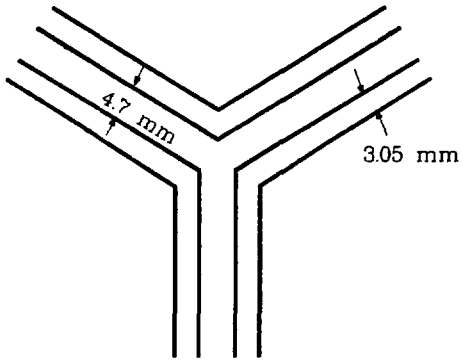

Fig. A-1. Three neighboring hexagonal subassembly duct corners.

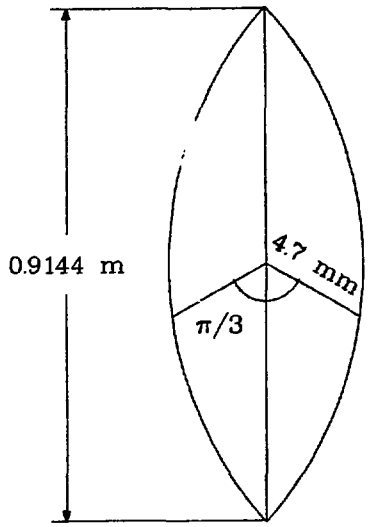

Fig. A-2. Fracture region boundary.

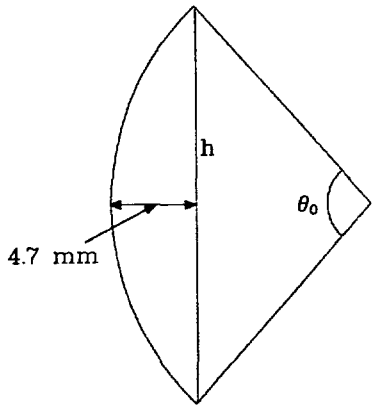

Fig. A-3. Calculational geometry for Eq. (A-1).

APPENDIX B

THERMAL STRESSES

We consider deformation of a solid body, a hexagonal subassembly duct modeled as a long cylindrical pipe, which is accompanied by a change in temperature. We regard the undeformed state of the cylinder to be at some temperature T_0 and without external forces. The stress tensor is given by

$$\sigma_{ij} = \frac{E}{1+\nu}\left(\varepsilon_{ij} + \frac{\nu}{1-2\nu}\varepsilon_{kk}\delta_{ij}\right) - K\,\alpha(T - T_0)\delta_{ij} \quad , \tag{B-1}$$

where ε_{ij} is the infinitesimal strain tensor, E is Young's modulus, ν is Poisson's ratio, K is the bulk modulus, and α is the thermal expansion coefficient. The last term gives the additional stresses caused by the temperature change.

The equation of equilibrium is

$$\frac{\partial \sigma_{ij}}{\partial x_j} = 0 \quad , \tag{B-2}$$

which is solved in cylindrical coordinates r,z (azimuthal symmetry) with boundary conditions

$$\left.\sigma_{rr}\right|_{r=R_1} = -P_1$$
$$\left.\sigma_{rr}\right|_{r=R_2} = -P_2 \quad , \tag{B-3}$$

where P_1 and P_2 are pressures exerted on the inside and outside of the cylinder, respectively. In addition, a temperature profile T = T(r) is assumed to exist in the cylinder.

The solution of this boundary value problem for the hoop stress is

$$\sigma_{\Theta\Theta} = \frac{R_1^2}{R_2^2 - R_1^2}\left(1 + \frac{R_2^2}{r^2}\right)P_1 - \frac{R_2^2}{R_2^2 - R_1^2}\left(1 + \frac{R_1^2}{r^2}\right)P_2$$

$$+ \frac{1-2\nu}{1-\nu} K\,\alpha\left[\frac{1}{r^2}\int_{R_1}^{r} dr' r' \Delta T(r') + \frac{1}{R_2^2 - R_1^2}\left(1 + \frac{R_1^2}{r^2}\right)\int_{R_1}^{R_2} dr' r' \Delta T(r') - \Delta T(r)\right], \tag{B-4}$$

where $\Delta T(r) \equiv T(r) - T_o$. This solution has the properties that: (1) if $P_1 = P_2 = 0$ and $T(r) = T_1$ (a constant), then $\sigma_{\theta\theta} = \sigma_{rr} = 0$ ($\sigma_{zz} \neq 0$ because no deformation is allowed in the z-direction); (2) if $R_{12}P_1 > R_{22}P_2$ (which implies $P_1 > P_2$ because $R_1 < R_2$), then the pressure contribution to $\sigma_{\theta\theta}$ is always positive, i.e., tensile.

Next consider a thin shell approximation to the above solution. Let $h = R_2 - R_1$, $2R = R_1 + R_2$ with $h/R \ll 1$. Also assume the temperature profile to be linear (Fig. B-1), i.e.,

$$T(r) = T_1 + \frac{T_2 - T_1}{R_2 - R_1}(r - R_1). \tag{B-5}$$

Finally let us write

$$r = R + \frac{fh}{2} \quad , \tag{B-6}$$

where fh is some positive or negative fraction of h, i.e., $-1 \leq f \leq 1$. Then Eq. (B-4) is approximated by

$$\sigma_{\theta\theta} \approx \frac{1 - \frac{fh}{2R}}{\frac{h}{R}}(P_1 - P_2) - \frac{(P_1 + P_2)}{2} - \frac{1 - 2\nu}{1 - \nu} K \alpha f \frac{T_2 - T_1}{2} + O(h). \tag{B-7}$$

The thermal stress contribution to the hoop stress is shown in Fig. B-2. It is easily seen that this calculation for $\sigma_{\theta\theta}$ is equivalent to heating the shell uniformly to a temperature $(T_1 + T_2)/2$, which induces no hoop stress, followed by increasing the temperature of the outer surface by $(T_2 - T_1)/2$ and decreasing the temperature of the inner surface by the same amount. This puts the outer half of the shell in compression and the inner half in tension; if $T_1 > T_2$, the compression and tension are reversed.

The pressure contribution to $\sigma_{\theta\theta}$ indicates that for most cases, if $P_1 > P_2$, the hoop stress will be tensile. Contradictions to this statement could occur if P_1 and P_2 are sufficiently large, but $P_1 \approx P_2$.

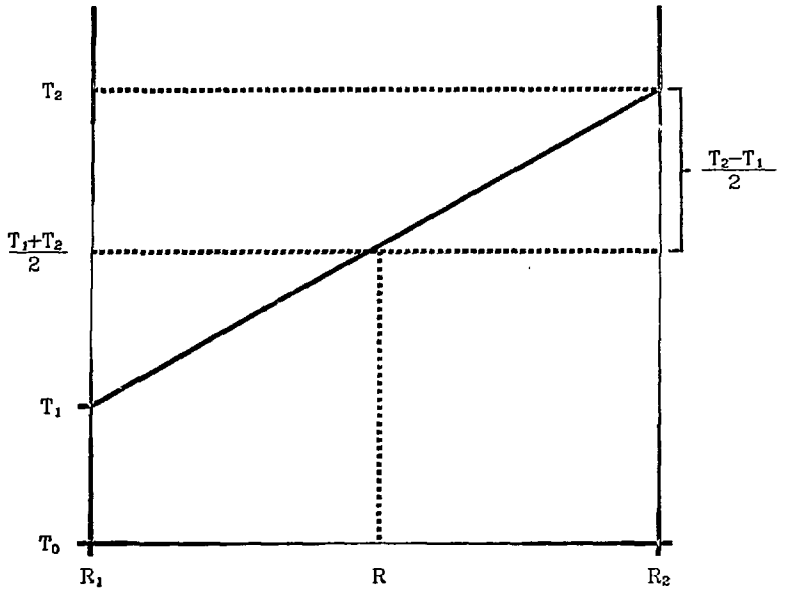

Fig. B-1.
Linear temperature profile.

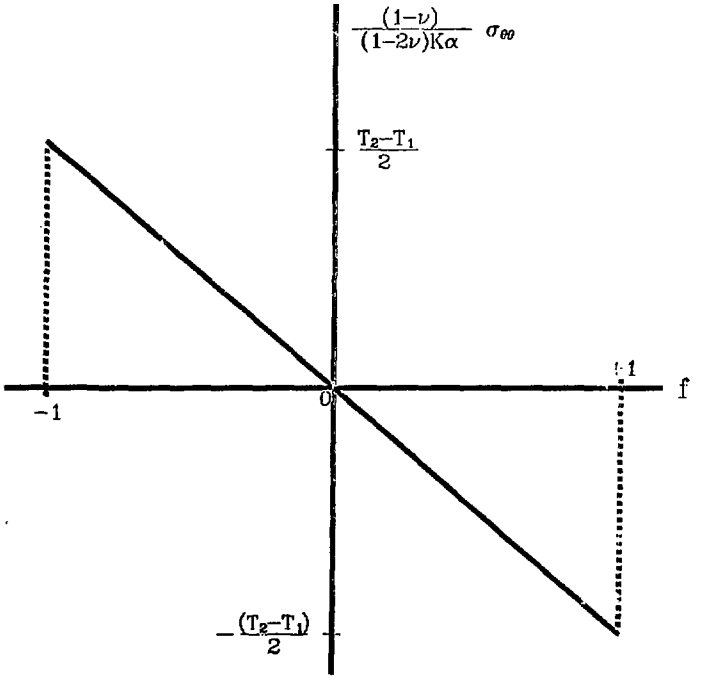

Fig. B-2.
Thermal stress caused by a linear temperature profile.

☆U.S. GOVERNMENT PRINTING OFFICE: 1982-0-376-020/138